

THE MASS DISTRIBUTION IN THE ELLIPTICAL GALAXY NGC 3377:
EVIDENCE FOR A 2×10^8 - M_{\odot} BLACK HOLE

JOHN KORMENDY,^{1,2,3} RALF BENDER,³ AARON S. EVANS,^{2,4} AND DOUGLAS RICHSTONE⁵

Received 1997 May 30; Accepted 1998, February 4

ABSTRACT

This paper is a study of the mass distribution in the central $35'' \simeq 1.7$ kpc of the E5 galaxy NGC 3377. Stellar rotation velocity and velocity dispersion profiles (seeing $\sigma_* = 0''.20 - 0''.56$) and V-band surface photometry ($\sigma_* = 0''.20 - 0''.26$) have been obtained with the Canada-France-Hawaii Telescope. NGC 3377 is kinematically similar to M32: the central kinematic gradients are steep. There is an unresolved central rise in rotation velocity to $V = 110 \pm 3$ km s⁻¹ (internal error) at $r = 1''.0$. The apparent velocity dispersion rises from 95 ± 2 km s⁻¹ at $1''.0 \leq r < 4''$ to 178 ± 10 km s⁻¹ at the center.

To search for a central black hole, we derive three-dimensional velocity and velocity dispersion fields that fit the above observations and *Hubble Space Telescope* surface photometry after projection and seeing convolution. Isotropic models imply that the mass-to-light ratio rises by a factor of ~ 4 at $r < 2''$ and $M/L_V \gtrsim 10$. If the mass-to-light ratio of the stars, $M/L_V = 2.4 \pm 0.2$, is constant with radius, then NGC 3377 contains a central massive dark object (MDO), probably a black hole, of mass $M_{\bullet} \simeq (1.8 \pm 0.8) \times 10^8 M_{\odot}$. Several arguments suggest that NGC 3377 is likely to be nearly isotropic. However, flattened, anisotropic maximum entropy models can fit the present data without an MDO. Therefore the MDO detection in NGC 3377 is weaker than those in M31, M32, and NGC 3115.

The above masses are corrected for the E5 shape of the galaxy and for the difference between velocity moments and velocities given by Gaussian fits to the line profiles. We show that the latter correction does not affect the strength of the MDO detection, but it slightly reduces M_{\bullet} and M/L_V .

At $3'' \lesssim r \lesssim 35''$, M/L_V is constant at ~ 2.4 . Therefore the inner parts of NGC 3377 are dominated by a normal old stellar population. In this elliptical, as in the bulge-dominated galaxies NGC 3115 and NGC 4594, halo dark matter is unimportant over a significant range in radius near the center.

1. INTRODUCTION

This paper is part of a search for supermassive black holes (BHs) in galaxy nuclei (see Kormendy 1992a, b, 1993; Kormendy & Richstone 1995, hereafter KR95; for reviews). There is a growing body of dynamical evidence for central dark objects of mass $10^{6.5} - 10^{9.5} M_{\odot}$ in galaxies. The simplest interpretation is that these are BHs that once were engines for nuclear activity. Most stellar-dynamical detections have been in relatively inactive bulges of disk galaxies (M31: Dressler 1984; Kormendy 1987a, 1988a, b; Dressler & Richstone 1988; Bacon *et al.* 1994, NGC 3115: Kormendy & Richstone 1992; Kormendy *et al.* 1996a, and NGC 4594: Kormendy 1988c; Emsellem *et al.* 1994; Kormendy *et al.* 1996b). In contrast, nuclear activity is strongest in giant ellipticals. The only ellipticals with stellar-dynamical evidence for BHs are the inactive dwarfs M32 (Tonry 1984, 1987; Dressler & Richstone 1988; van der Marel *et al.* 1994b; Qian *et al.* 1995; Dehnen 1995; Bender, Kormendy, & Dehnen 1996; van der Marel *et al.* 1997a, b) and NGC 4486B (Kormendy *et al.* 1997). However, failure to detect BHs is not evidence against them. Gas-dynamical searches have found BHs in six

galaxies, three of which are active giant ellipticals (Harms *et al.* 1994; Ferrarese *et al.* 1996; Bower *et al.* 1998). In fact, any giant elliptical could hide a 10^8 - M_{\odot} BH from past stellar-dynamical searches.

The BH search is becoming dominated by the *Hubble Space Telescope* (*HST*); with it, BH detection is possible in most giant galaxies out to the distance of the Virgo cluster. But for ground-based searches, BH detection is difficult. There are two main reasons. First, giant ellipticals do not rotate, so mass measurements are maximally sensitive to velocity anisotropies. Second (e.g., Lauer *et al.* 1995), they have cuspy cores with large break radii; inside r_b the brightness profile is relatively shallow, so projected spectra are dominated by light from large radii where a BH has no effect. Kormendy (1992b) illustrates this effect for the *HST* profile of M87.

The BH in M32 was found because the galaxy is nearby and rapidly rotating. Similarly, M31, NGC 3115, and NGC 4594 contain rapidly rotating nuclear disks. They are nearly edge-on; this ensures that spatially unresolved rotation contributes to the apparent velocity dispersion. Finally, a detection was possible in NGC 4486B because the BH is unusually massive compared to the rest of the galaxy. Ground-based BH detection is still only possible in galaxies like these where circumstances are favorable.

NGC 3377 is such a galaxy. It is a prototypical E5 galaxy illustrated in the *Hubble Atlas* (Sandage 1961). At $M_B = -18.8$, it is just fainter than the transition between ellipticals that rotate and those that do not: it rotates rapidly enough to be nearly isotropic (Davies *et al.* 1983). Also, it has a coreless, power-law profile (Lauer *et al.* 1995), so small radii have large luminosity weight in projection. The axial ratio is 0.5; since no

¹ Visiting Astronomer, Canada-France-Hawaii Telescope, operated by the National Research Council of Canada, the Centre National de la Recherche Scientifique of France, and the University of Hawaii.

² Institute for Astronomy, University of Hawaii, 2680 Woodlawn Dr., Honolulu, HI 96822; Electronic mail: kormendy@ifa.hawaii.edu

³ Universitäts-Sternwarte, Scheinerstraße 1, München 81679, Germany; Electronic mail: bender@usm.uni-muenchen.de

⁴ Present address: Caltech 105-24, Pasadena, CA 91125; Electronic mail: ase@astro.caltech.edu

⁵ Department of Astronomy, University of Michigan, Ann Arbor, MI 48109; Electronic mail: dor@astro.lsa.umich.edu

elliptical is much flatter (Sandage, Freeman, & Stokes 1970; Binney & de Vaucouleurs 1981; Franx, Illingworth, & de Zeeuw 1991; Tremblay & Merritt 1995), NGC 3377 must have a high inclination. We assume that it is edge-on. Finally, NGC 3377 is one of the nearest ellipticals. It is therefore an excellent target for a BH search. This paper presents high-resolution surface photometry and stellar-kinematic measurements and uses them to calculate the mass-to-light ratio M/L_V as a function of radius. NGC 3377 turns out to be kinematically similar to M32. Isotropic models imply that it contains a BH of mass $M_\bullet \simeq 1.8 \times 10^8 M_\odot$.

We also discuss the mass distribution at $3'' \lesssim r \lesssim 35''$. Mass distributions have been measured in only a few bulges and ellipticals. At radii well outside the de Vaucouleurs (1948) effective radius r_e , a variety of techniques show that halo dark matter dominates the mass distribution (see Kent 1990 for a review). Mass-to-light ratios $M/L_V \sim 10^2$ are large compared to values $M/L_V \lesssim 10$ for old stellar populations. Measurements at $r \lesssim r_e$ need to be more accurate. Variations in M/L_V due to metallicity gradients, halo dark matter and all but the most spectacular BHs are likely to be smaller than a factor of 2 to 4. Measurements intended to be this precise are vulnerable to velocity anisotropies. Only a few well-studied galaxies are likely to be isotropic or else contain embedded, edge-on disks that simplify the measurements without contributing much mass (e.g., NGC 3115 and NGC 4594, see Kormendy & Westpfahl 1989 for the latter). The observed result is that these galaxies have $M/L_V \simeq$ constant near their centers. Moreover, M/L_V is small, so the mass is dominated by an old stellar population and not by halo dark matter. Here we show that this is also the case in NGC 3377.

We assume that the distance to NGC 3377 is 9.9 Mpc based on a Hubble constant of $H_0 = 80 \text{ km s}^{-1} \text{ Mpc}^{-1}$, the recession velocity $626 \pm 39 \text{ km s}^{-1}$ of the Leo Spur (Group 15 -1 in Tully 1988) and a Virgocentric flow solution (Faber *et al.* 1997). Then the scale is $20''.8 \text{ kpc}^{-1}$. The Galactic absorption is assumed to be $A_B = 0.06$ (Burstein & Heiles 1984).

2. KINEMATICS

2.1. Observations and Data Reduction

The kinematic measurements were made during four observing runs with the Canada-France-Hawaii Telescope. For the first two runs, the Herzberg Spectrograph (Salmon 1985) was used at f/4 with an RCA CCD (316×498 , $30 \mu\text{m}$ pixels; read noise $\sim 71 \text{ e}^{-1} \text{ pixel}^{-1}$; Walker *et al.* 1984). Spectra were taken at position angles $\text{PA} = 50^\circ$ and 44° . Leach (1981) measured these as the PAs of the major axis at small and moderate radii. Subsequently, we found that our photometry shows no twist near the center. Present and published CCD photometry (§ 3) imply that the major axis is at $\text{PA} = 41^\circ \pm 1^\circ$ (external error). We neglect the small difference between the correct major-axis PA and that of the spectra.

For subsequent runs, we used the Subarcsecond Imaging Spectrograph (SIS). Tip-tilt guiding is incorporated; by offsetting the guide probe, we can center the object on the slit to one-pixel accuracy. An observing sequence consists of a series of direct images to center the object at the slit, an exposure with the slit in place but with no grism, the object spectrum, another image through the slit but without the grism and one with neither slit nor grism to verify that the object is still centered, and a comparison spectrum. The seeing was measured on the bracketing direct images. The brightness profile of the galaxy is the same in these images and in the spectrum, so the PSF in the images is correct for the spectrum.

Parameters of the spectra are given in Table 1. Integration times, position angles, and seeing estimates are given in Table 2.

Atmospheric dispersion was negligible. The centering exposures were taken with an I filter and the same CCD that was used for the spectroscopy, so the effective wavelength was close to that of the Ca triplet. Also, the mean zenith distances were $24^\circ.3$ for spectrum 77f707, $6^\circ.0$ for spectrum 78f873, and $7^\circ.5$ for spectrum 80f027. The BH models were fitted to spectrum 80f027.

TABLE 1
PARAMETERS OF SPECTRA

Parameter	Run 1	Run 2	Run 3	Run 4
Dates of observations	1986 Dec. 25–28	1987 Mar. 20–25	1994 Apr. 18–21	1996 Apr. 25–27
Spectrograph	Herzberg	Herzberg	SIS	SIS
Spectra (Table 2)	29f56	33f26	74f770	77f707, 78f873, 80f027
Slit length	2'0	2'0	2'5	2'8
Scale along slit	0''44 pixel ⁻¹	0''44 pixel ⁻¹	0''0864 pixel ⁻¹	0''15 pixel ⁻¹
Slit width	0''5	0''5	0''26	0''37
Wavelength range	5067–5667 Å	5064–5684 Å	7975–8975 Å	7580–9405 Å
Reciprocal dispersion	1.17 Å pixel ⁻¹	1.22 Å pixel ⁻¹	0.977 Å pixel ⁻¹	1.781 Å pixel ⁻¹
Reciprocal dispersion	66 km s ⁻¹ pixel ⁻¹	68 km s ⁻¹ pixel ⁻¹	34.6 km s ⁻¹ pixel ⁻¹	63.3 km s ⁻¹ pixel ⁻¹
Comparison line FWHM	1.7 pixel	1.8 pixel	2.54 pixel	2.19 pixel
Instrumental velocity dispersion	48 km s ⁻¹	51 km s ⁻¹	37 km s ⁻¹	59 km s ⁻¹
Standard star	γ Tau	η Cyg	η Cyg, κ Oph, μ Leo, γ Dra	η Cyg, κ Oph, γ Dra
Standard star spectral type	K0 III	K0 III	K0 III, K2 III, K2 III, K5 III	K0 III, K2 III, K5 III

NOTE. – The spatial resolution of the Herzberg Spectrograph is limited approximately equally by the spectrograph camera and by seeing.

Instrumental reduction of RCA CCD data is routine. The spectra were corrected for geometric distortion and rewritten on a $\ln \lambda$ scale using the “longslit” package in the National Optical Astronomy Observatories’ *Image Reduction and Analysis Facility* (Tody *et al.* 1986).

Spectra of MK standard stars chosen from Morgan & Keenan (1973) were observed and reduced similarly. Since their images were smaller than the slit, stars were trailed along the slit at position angles slightly different from 0° or 90° . After rectification, intensities were averaged along the slit to produce one-dimensional spectra with the proper instrumental dispersion. In the Fourier analysis, different K0–5 III stars gave almost identical results. The adopted star(s) (Table 1) gave marginally the best internal and external consistency.

Velocities V and velocity dispersions σ were calculated using a Fourier quotient program (Sargent *et al.* 1977; Schechter & Gunn 1979) as discussed in Kormendy & Illingworth (1982) and in Kormendy & Richstone (1992). Results are listed in Table 2. The adopted center is determined with an accuracy of ~ 0.1 pixel by comparing the brightness profile along the slit with the surface photometry discussed in §3. The rotation curves measured from the Run 4 spectra are slightly asymmetric; the results in Table 2 contain a shift of $\Delta r = 0''.15$ applied to all radii. It is not clear whether this is real (as in M31) or not. It is difficult to believe that it could be due to an undiagnosed problem with centering or guiding, because the brightness profile along the slit provides a check on both. We will not

attempt to interpret the asymmetry; it is small enough that it does not affect our conclusions.

2.2. A First Look at the Kinematics

Figure 1 illustrates the kinematics. The rotation and dispersion profiles closely resemble those of M32 (Tonry 1984, 1987; Kormendy 1987a; Dressler & Richstone 1988; Carter & Jenkins 1993; van der Marel *et al.* 1994a; Bender, Kormendy, & Dehnen 1996; van der Marel, de Zeeuw, & Rix 1997). The kinematic gradients near the center are unresolved. The maximum rotation velocity $V = 110 \pm 3$ km s $^{-1}$ (internal error) has already been reached $1''.0$ from the center. The velocity dispersion increases by 87% from 95 ± 2 km s $^{-1}$ at $1''.0 \leq r < 4''$ to 178 ± 10 km s $^{-1}$ at the center. As in M32, V and σ continue to decrease slowly at large radii.

Our value of the central dispersion is somewhat larger than $\sigma = 160$ km s $^{-1}$ adopted by Whitmore, McElroy, & Tonry (1985) based on three published measurements. We also find a larger maximum rotation velocity than the value 80 ± 6 km s $^{-1}$ quoted by Davies *et al.* (1983) based on measurements in Illingworth (1977). The difference is due to the lower resolution of the photographic spectra available in 1977. Figure 1 shows that the maximum rotation velocity, the apparent central velocity dispersion, and the central gradients in V and σ all get larger as resolution improves.

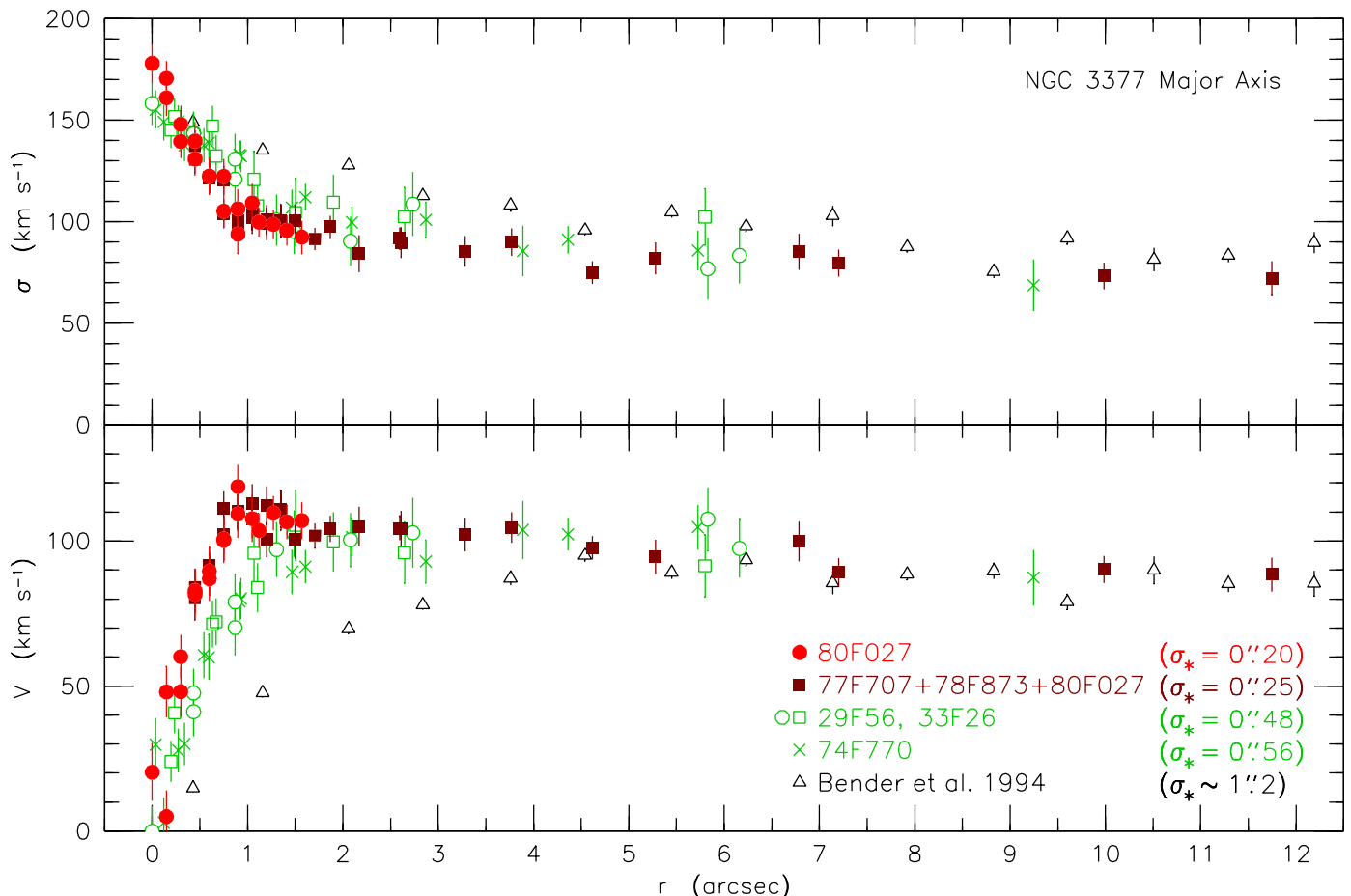


FIG. 1.—Folded rotation curve and dispersion profile along the major axis of NGC 3377. Central points of SIS spectrum 80f027 are separated by $0''.15$.

TABLE 2
ROTATION AND VELOCITY DISPERSION DATA

NGC 3377 Spectrum 29f56				
Exp. = 1800 s PA = 44° $\sigma_* = 0''49$				
r	V	$\epsilon(V)$	σ	$\epsilon(\sigma)$
-5.8	108	11	77	15
-2.1	100	9	90	12
-1.3	97	9	101	13
-0.9	70	10	121	12
-0.4	41	8	144	11
0.0	0	9	158	11
0.4	-48	8	143	11
0.9	-79	10	131	13
1.5	-103	8	95	11
2.7	-103	12	109	16
6.2	-97	10	83	14

NGC 3377 Spectrum 33f26				
Exp. = 1800 s PA = 50° $\sigma_* = 0''47$				
r	V	$\epsilon(V)$	σ	$\epsilon(\sigma)$
-2.6	96	11	103	14
-1.5	105	12	105	17
-1.1	96	11	121	14
-0.6	71	8	147	10
-0.2	24	7	145	9
0.2	-41	7	152	9
0.7	-72	8	132	10
1.1	-84	8	108	11
1.9	-100	10	110	14
5.8	-91	11	102	14

NGC 3377 Major Axis 74f770				
Exp. = 3600 s P.A. = 41° $\sigma_* = 0''56$				
r	V	$\epsilon(V)$	σ	$\epsilon(\sigma)$
-15.02	90	10	82	14
-5.73	105	8	86	10
-3.89	104	10	86	12
-2.87	93	7	101	9
-1.61	91	6	112	7
-0.93	80	7	132	8
-0.59	60	8	139	8
-0.34	30	7	138	8
-0.12	3	9	149	9
0.04	-30	9	155	9
0.27	-28	8	149	8
0.54	-61	8	138	8
0.92	-79	7	133	7
1.47	-89	8	107	9
2.09	-101	6	100	7
4.36	-102	6	91	7
9.25	-87	10	69	13

NGC 3377 Spectrum 80f027				
Exp. = 1800 s PA = 40° $\sigma_* = 0''20$				
r	V	$\epsilon(V)$	σ	$\epsilon(\sigma)$
-2.06	109	6	79	9
-1.80	110	10	101	12
-1.57	107	6	92	8
-1.27	110	6	99	7
-1.05	108	8	109	9
-0.90	109	8	106	10
-0.75	101	7	105	8
-0.60	87	8	122	8
-0.45	83	8	131	8
-0.30	60	8	139	8
-0.15	48	9	171	9
0.00	20	10	178	10
0.15	-5	9	161	9
0.30	-48	9	148	9
0.45	-82	9	140	9
0.60	-90	8	122	9
0.75	-100	8	122	9
0.90	-119	8	94	9
1.12	-104	6	100	7
1.41	-107	6	96	7
1.85	-99	5	92	7

NGC 3377 Spectra 77f707+78f873+80f027				
Exp. = 5400 s PA = 40° $\sigma_* \simeq 0''25$				
r	V	$\epsilon(V)$	σ	$\epsilon(\sigma)$
-20.99	92	7	66	12
-11.75	88	6	72	8
-7.20	89	5	80	7
-4.62	98	4	75	6
-3.29	102	6	85	8
-2.61	104	6	90	8
-2.17	105	7	84	9
-1.71	102	4	92	5
-1.35	111	7	100	8
-1.20	112	7	99	8
-1.05	108	7	102	8
-0.90	110	6	101	8
-0.75	111	6	104	7
-0.60	92	6	122	7
0.60	-89	7	122	7
0.75	-102	7	121	7
0.90	-110	6	99	8
1.05	-113	7	104	8
1.20	-100	6	101	7
1.35	-111	6	100	8
1.50	-101	7	101	8
1.87	-104	5	98	6
2.60	-104	4	92	5
3.77	-105	5	90	7
5.28	-94	6	82	8
6.79	-100	7	85	9
9.98	-90	5	73	7
22.65	-86	11	83	14

NOTE. – The photometric major axis is at PA = 41° ± 1°.

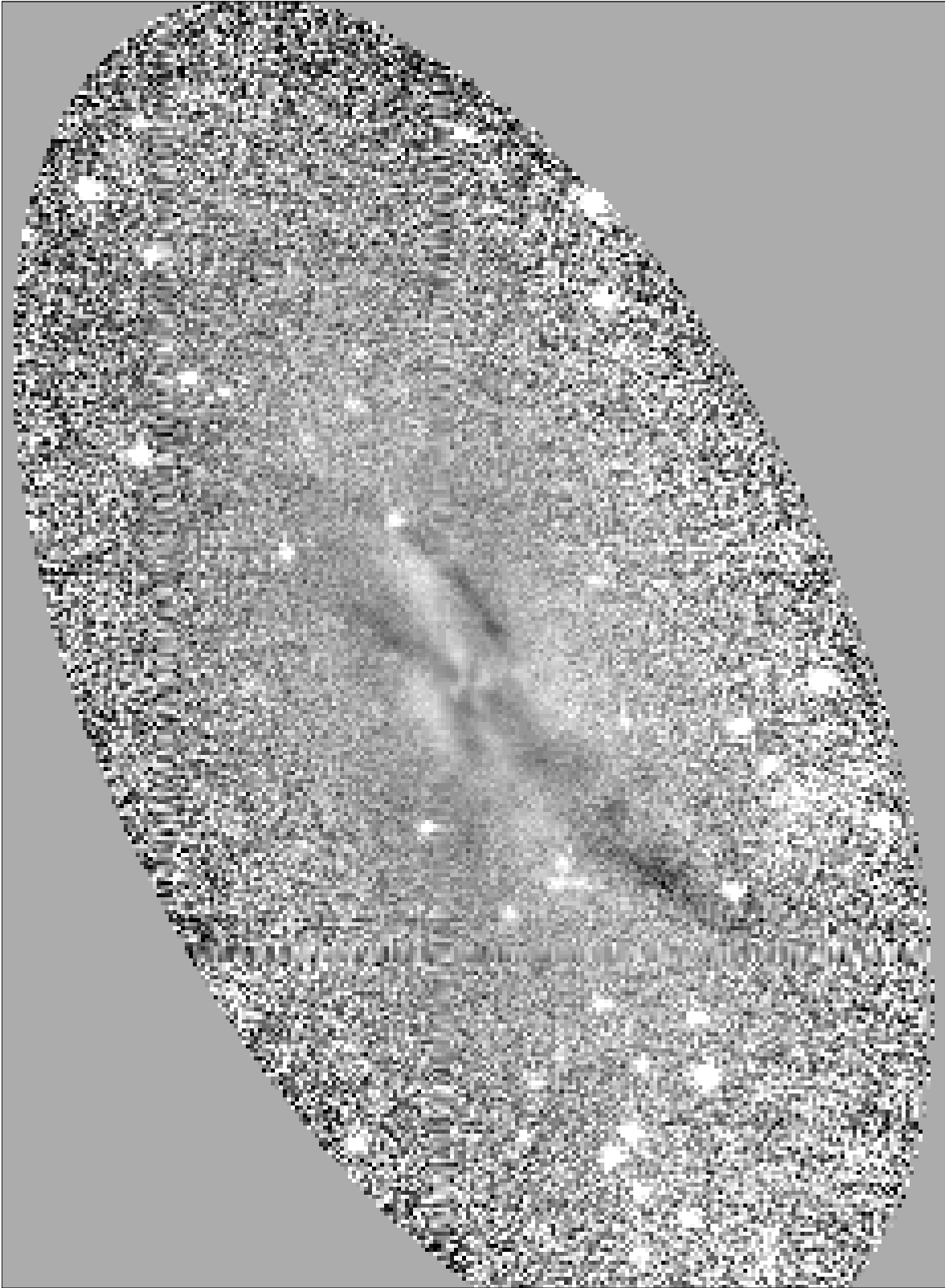


FIG. 2.—Unsharp-masked, V -band image of NGC 3377. This is image 5f57 in Table 3, i.e., a 180 s exposure with seeing $\sigma_* = 0''.26$. Inside the outermost contour for which the brightness profile was calculated, the image was divided by a reconstruction that has exactly elliptical isophotes and the galaxy’s measured brightness, ellipticity, and PA profiles. Outside this contour, the image is set equal to 1. The grayscale is linear between 0.8 (black) and 1.1 (white). Most dust patches are a few percent deep; the strongest absorption is 8%. Note that the appearance of diskiness is enhanced by the geometry of the dust distribution. The area shown is $1'.13$ high and $0'.83$ wide. North is 16° clockwise from upward, and east is 16° clockwise from left.

3. PHOTOMETRY

Four V -band images of NGC 3377 were obtained at the CFHT Cassegrain focus with the RCA CCD (scale = $0''.215$ pixel $^{-1}$). Results are listed in Table 3. For images 5f54 – 5f57, the quoted seeing is an average for 0, 1, 3, and 9 stars, respectively, scattered around the galaxy on the frames. No star is bright enough for the shortest exposure, 5f54. However, Figure 4 (below) clearly shows that the seeing was better than for 5f55, which has a well measured $\sigma_* = 0''.22$. Also, at the time of the observations (1984 March), the best images ever obtained with the CFHT had $\sigma_* \simeq 0''.19$ (FWHM $\simeq 0''.45$). Therefore we adopt $\sigma_* = 0''.20 \pm 0''.01$.

CCD photometry of large galaxies is usually limited by the accuracy of sky subtraction. Here, too, the galaxy image is larger than the chip. For all four images, we adopt the median sky brightness in a 900 s exposure on a blank field taken immediately after image 5f57. We also measured median brightnesses at the corners of the galaxy exposures (in each case, NGC 3377 is close to the center). The ratios of these brightnesses to the adopted sky values are 1.18, 1.17 ± 0.06 , 1.16 ± 0.01 , and 1.17 ± 0.01 for 5f54 – 5f57, respectively. This consistency implies that the sky brightness did not vary significantly during the 35 m course of the galaxy and sky exposures. For images 5f54 – 5f57, Table 3 lists profiles out to only 2.7 – 1.1 times the sky brightness. We have not tried to measure NGC 3377 to faint levels because the sky brightness is less certain than if it were measured on the object images. We will in any case use a composite profile that at large radii is based on photometry with large-field CCDs. Also, our analysis is insensitive to the outer profile.

The profiles were calculated using a slightly modified form of the PROFILE program in the Lick Observatory image processing system VISTA (Stover 1988). PROFILE was written by T. Lauer (1985). It uses sinc interpolation optimized for high spatial resolution and is remarkably accurate. Even test profiles observed with 2 – 3 pixels per FWHM are well measured.

PROFILE fits elliptical isophotes to the image. Since real isophotes in many elliptical galaxies show disk or boxy distortions, we checked that the above procedure adequately measures the major-axis profile. Figure 2 shows an “unsharp-masked” version of image 5f57. A synthetic image was constructed with exactly elliptical isophotes and the measured brightness, ellipticity, and PA profiles. Image 5f57 was divided by this synthetic image to produce Figure 2. The cross-shaped pattern is the signature of a disk distortion (Carter 1987; Jedrzejewski 1987; Michard & Simien 1988; Bender, Döbereiner, & Möllenhoff 1988; Nieto & Bender 1989; Peletier *et al.* 1990; Nieto *et al.* 1991; Scorza & Bender 1995); this is normal for an elliptical galaxy that rotates rapidly (Bender 1988; Nieto, Capaccioli, & Held 1988; Nieto & Bender 1989; Bender *et al.* 1989; Kormendy & Bender 1996). Most of the light in the disk distortion is included in the profile; the residuals are too small to affect our analysis. Figure 2 also shows an irregular distribution of dust, but the amount of absorption is too small to be important here.

The zeropoint of the V magnitude scale is based on published aperture photometry by Webb (1964); Strom *et al.* (1976); Sandage & Visvanathan (1978); Persson, Frogel, & Aaronson (1979); Caldwell (1983), and Poulain (1988). Ten measurements with aperture radii of $11''.5$ to $30''.5$ were used. One measurement by Webb through a $12''.3$ aperture was discarded; it appears imperfectly centered.

For each measurement, synthetic aperture photometry on image 5f57 gave an instrumental magnitude. The difference between this and the published magnitude is the zeropoint. Zeropoints were found to be independent of aperture radius. Results from different papers are remarkably consistent: the mean of ten zeropoint determinations has an accuracy of ± 0.004 mag. We applied the zeropoint from image 5f57 to the other images by shifting the profiles in μ to minimize the scatter. We also checked that zeropoints calculated from the individual images are consistent. For images 5f54 – 5f56, they differ from the adopted zeropoint by 0.002, 0.025, and 0.002 mag arcsec $^{-2}$, respectively. Table 3 lists the brightness profiles with 5f57 zeropoints applied. Major-axis radius r is in arcsec, μ_V is in V mag arcsec $^{-2}$, ϵ is ellipticity, and PA is position angle in degrees east of north.

We verified that, except for resolution differences, the galaxy brightness profile is the same on the spectra and on the images.

Figure 3 shows the results. Also shown is photometry by Jedrzejewski (1987), Michard & Simien (1988), Peletier *et al.* (1990), and Pierce (1991). *HST* WFPC1 photometry from Lauer *et al.* (1995) provides the profile near the center. Figure 3 is the most accurate composite profile we can derive from available data; the published profiles are truncated at small radii where they “peel off” because of low resolution. The profiles by Jedrzejewski (1987) and by Peletier *et al.* (1990) are also truncated at large radii because of deviations due to inaccurate sky subtraction. The best data at large radii are those by Pierce and by Michard and Simien. Pierce used an 800×800 pixel TI CCD at the University of Hawaii 2.2 m telescope; the scale was $0''.6$ pixel $^{-1}$ and the unvignetted field was $5' \times 5'$. The sky was determined at the corners of the images; sky subtraction should be more accurate than for the other CCD photometry. Michard and Simien took photographic plates at the 1.2 m telescope of the Observatoire de Haute-Provence. The CCD data are preferred at small radii, but the photographic profile is probably the most accurate at large radii.

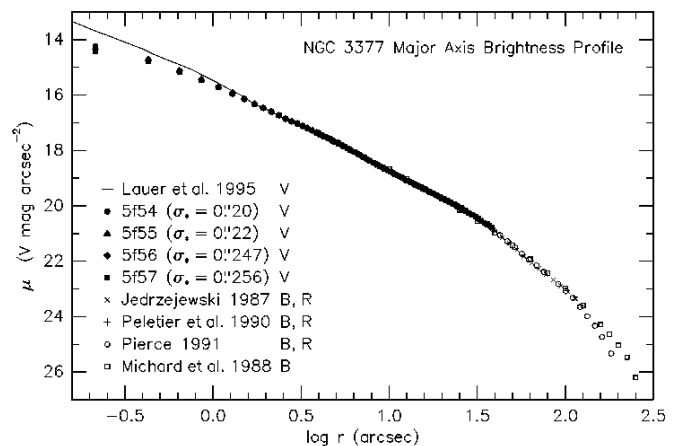


FIG. 3.—Major-axis brightness profile of NGC 3377. Sources of the published photometry are given in the key; “ B, R ” means that B - and R -band profiles have been intensity-averaged to approximate V . Since points are not distinguishable at $\log r < 1.6$, we note that the log radius range of the plotted data is: for Jedrzejewski (1987), 0.81 – 2.06; for Peletier *et al.* (1990), 0.51 – 1.40; for Pierce (1991), 0.85 – 2.26; and for Michard & Simien (1988), 1.00 – 2.40. Points omitted because of poor seeing or sky subtraction are included in Figure 4.

TABLE 3

NGC 3377 BRIGHTNESS PROFILE

5f54: Exp. = 20 s; $\sigma_* \simeq 0''.20$				5f55: Exp. = 30 s; $\sigma_* = 0''.22$			
r	μ_V	ϵ	PA	r	μ_V	ϵ	PA
0.00	13.997	0.097	44.50	0.00	14.104	0.174	44.18
0.22	14.237	0.097	44.50	0.22	14.297	0.174	44.18
0.43	14.716	0.173	44.50	0.43	14.721	0.200	44.18
0.64	15.121	0.251	44.50	0.64	15.119	0.255	44.18
0.86	15.449	0.313	45.42	0.86	15.438	0.316	45.18
1.07	15.719	0.363	44.23	1.08	15.700	0.364	43.98
1.29	15.927	0.409	43.83	1.29	15.927	0.399	43.39
1.50	16.145	0.427	43.70	1.50	16.142	0.419	43.33
1.72	16.317	0.442	43.42	1.72	16.315	0.436	43.25
1.94	16.468	0.452	43.16	1.94	16.472	0.442	43.22
2.15	16.606	0.461	43.01	2.15	16.603	0.454	42.70
2.37	16.726	0.471	42.12	2.37	16.735	0.460	42.62
2.58	16.847	0.474	42.05	2.58	16.850	0.468	41.85
2.80	16.941	0.483	41.53	2.80	16.943	0.481	41.56
3.01	17.040	0.487	41.48	3.01	17.033	0.490	41.30
3.23	17.114	0.501	41.45	3.23	17.127	0.495	41.27
3.44	17.199	0.505	41.35	3.44	17.194	0.509	41.18
3.65	17.281	0.514	41.35	3.65	17.268	0.516	41.18
3.87	17.357	0.515	41.35	3.87	17.345	0.519	41.18
4.19	17.453	0.524	41.31	4.09	17.418	0.522	41.18
4.62	17.585	0.528	41.23	4.30	17.489	0.523	41.12
5.05	17.700	0.532	41.27	4.51	17.557	0.524	41.23
5.48	17.836	0.529	41.93	4.73	17.623	0.526	41.23
6.02	17.977	0.521	42.31	4.95	17.686	0.524	41.29
6.67	18.123	0.510	42.32	5.16	17.743	0.524	41.44
7.42	18.302	0.495	42.22	5.48	17.831	0.524	41.58
8.38	18.471	0.499	41.77	6.02	17.977	0.517	42.02
9.46	18.661	0.489	41.31	6.67	18.142	0.503	42.34
10.64	18.830	0.498	40.87	7.31	18.285	0.494	42.24
13.29	19.145	0.496	40.16	7.96	18.415	0.492	41.86
15.49	19.384	0.491	40.83	8.60	18.533	0.490	41.42
16.76	19.483	0.496	40.57	9.46	18.678	0.487	41.08
18.81	19.643	0.499	37.39	10.53	18.816	0.496	40.44
20.74	19.780	0.499	34.70	14.08	19.253	0.491	40.60
				15.05	19.334	0.497	40.46
				22.79	19.900	0.512	40.63
				24.62	20.016	0.512	40.34

TABLE 3 — *Continued*

NGC 3377 BRIGHTNESS PROFILE

5f56: Exp. = 60 s; $\sigma_* = 0''.247 \pm 0''.005$				5f56: Exp. = 60 s; $\sigma_* = 0''.247 \pm 0''.005$			
r	μ_V	ϵ	PA	r	μ_V	ϵ	PA
0.00	14.151	0.154	44.29	15.60	19.373	0.501	40.90
0.22	14.334	0.154	44.29	16.44	19.443	0.507	40.66
0.43	14.744	0.176	44.29	17.31	19.528	0.500	40.62
0.64	15.134	0.233	44.29	18.18	19.593	0.502	40.76
0.86	15.452	0.300	45.27	19.03	19.657	0.506	40.86
1.08	15.710	0.354	43.98	19.88	19.724	0.505	40.90
1.29	15.939	0.387	43.63	20.75	19.779	0.507	40.65
1.50	16.144	0.409	43.56	21.71	19.843	0.512	40.77
1.72	16.317	0.426	43.54	22.79	19.922	0.511	41.28
1.94	16.461	0.441	43.53	23.98	19.994	0.509	41.05
2.15	16.600	0.449	43.42	25.26	20.073	0.510	41.30
2.37	16.729	0.455	42.71	26.55	20.161	0.511	40.94
2.58	16.847	0.464	42.02	27.84	20.230	0.510	42.02
2.80	16.940	0.478	41.59	29.13	20.302	0.510	41.85
3.01	17.032	0.488	41.54	35.59	20.647	0.511	40.46
3.23	17.118	0.497	41.53	36.86	20.724	0.501	40.76
3.44	17.194	0.506	41.30	38.04	20.764	0.500	40.22
3.65	17.271	0.512	41.15				
3.87	17.351	0.513	41.14				
4.09	17.415	0.518	41.14				
4.41	17.520	0.521	41.22				
4.84	17.651	0.524	41.35				
5.27	17.772	0.524	41.58				
5.70	17.886	0.523	41.95				
6.13	18.009	0.510	42.21				
6.56	18.109	0.505	42.44				
6.99	18.214	0.497	42.39				
7.63	18.354	0.490	42.16				
8.38	18.497	0.486	41.83				
9.03	18.595	0.491	41.60				
9.68	18.692	0.494	41.26				
10.43	18.803	0.494	40.84				
11.28	18.919	0.494	40.46				
12.15	19.023	0.494	40.32				
13.01	19.132	0.493	40.43				
13.87	19.226	0.492	40.54				
14.73	19.306	0.493	40.62				

TABLE 3 — *Continued*

NGC 3377 BRIGHTNESS PROFILE

5f57: Exp. = 180 s; $\sigma_* = 0''.256 \pm 0''.007$				5f57: Exp. = 180 s; $\sigma_* = 0''.256 \pm 0''.007$			
r	μ_V	ϵ	PA	r	μ_V	ϵ	PA
0.00	14.263	0.148	45.04	10.85	18.861	0.490	40.67
0.22	14.420	0.148	45.04	11.72	18.972	0.491	40.38
0.43	14.782	0.174	45.04	12.57	19.076	0.491	40.32
0.64	15.152	0.225	45.04	13.44	19.169	0.494	40.43
0.86	15.462	0.285	46.39	14.30	19.254	0.496	40.65
1.08	15.724	0.330	44.88	15.16	19.335	0.497	40.71
1.29	15.947	0.368	43.84	16.01	19.408	0.500	40.73
1.50	16.150	0.393	43.59	16.88	19.483	0.501	40.54
1.72	16.321	0.413	43.38	17.74	19.551	0.504	40.56
1.94	16.473	0.427	43.18	18.60	19.609	0.509	40.66
2.15	16.607	0.437	43.05	19.45	19.676	0.506	40.74
2.37	16.730	0.447	43.04	20.32	19.738	0.507	40.81
2.58	16.841	0.457	42.28	21.28	19.800	0.511	40.89
2.80	16.943	0.468	41.74	22.36	19.866	0.513	41.18
3.01	17.030	0.480	41.38	23.33	19.937	0.512	40.97
3.23	17.118	0.488	41.22	24.41	19.999	0.513	40.94
3.44	17.198	0.496	41.20	25.69	20.080	0.513	40.96
3.65	17.276	0.502	41.20	26.98	20.158	0.511	41.15
3.87	17.352	0.506	41.20	28.27	20.245	0.507	41.47
4.09	17.426	0.509	41.22	29.56	20.311	0.508	41.33
4.30	17.492	0.513	41.31	30.87	20.391	0.506	40.97
4.51	17.555	0.516	41.42	32.15	20.460	0.507	40.96
4.73	17.620	0.518	41.42	33.43	20.538	0.503	40.91
4.95	17.681	0.520	41.44	34.73	20.599	0.502	41.06
5.16	17.742	0.520	41.48	36.02	20.660	0.503	40.88
5.38	17.801	0.520	41.66	37.28	20.724	0.499	40.75
5.59	17.861	0.518	41.97	38.37	20.786	0.490	40.60
5.81	17.923	0.513	42.08				
6.02	17.976	0.512	42.15				
6.35	18.059	0.505	42.32				
6.78	18.164	0.497	42.32				
7.20	18.256	0.493	42.27				
7.64	18.348	0.489	42.15				
8.17	18.450	0.487	42.05				
8.81	18.560	0.488	41.85				
9.46	18.660	0.488	41.32				
10.11	18.760	0.488	41.17				

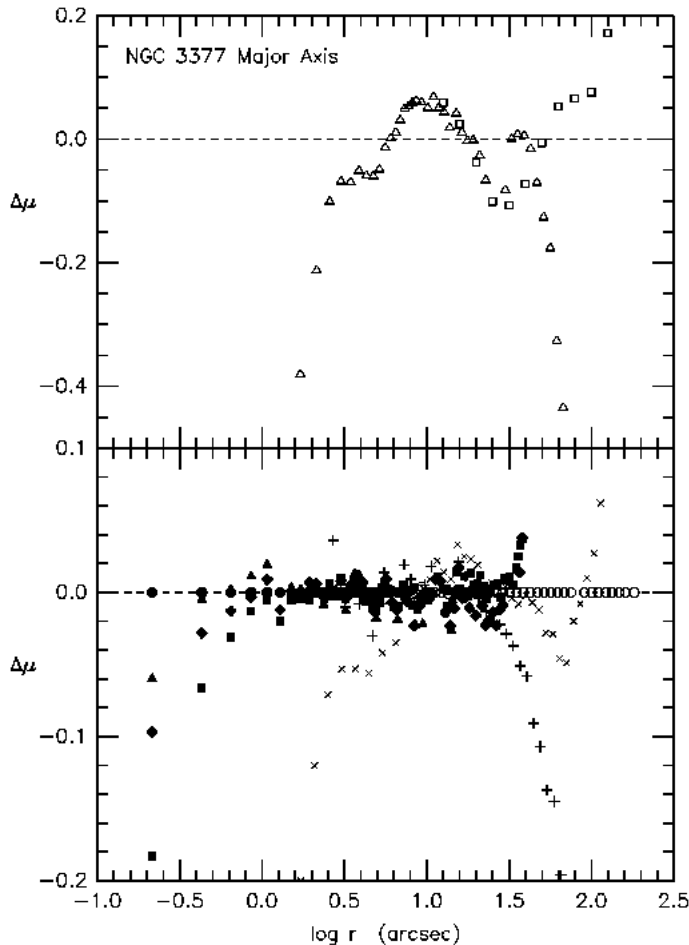


FIG. 4.—Deviations $\Delta\mu$ (mag arcsec^{-2}) of the individual profiles in Figure 3 from the 5f54 profile at small r and the Pierce (1991) profile at large r . The lower panel shows the most accurate photometry; the upper panel shows the rest of the data. The symbols are the same as in Figure 3 except that open triangles are r -band data from Djorgovski (1985). Near the center, points “peel away” from $\Delta\mu = 0 \text{ mag arcsec}^{-2}$ where profiles have lower spatial resolution than $\sigma_* = 0''.20$. Deviations at large radii are assumed to be due to inaccurate sky subtraction.

In § 5, we derive volume brightness models that fit these data after projection and seeing convolution. To illustrate the precision we should aim for, we show in Figure 4 the deviations of the photometry from an average of the 5f54 profile at small r and the Pierce profile at large r . This time, all of the above photometry is included, so deviations at small and large radii are apparent. The upper panel shows the Michard & Simien (1988) data and photometry by Djorgovski (1985). The latter were derived with a CCD that is poor by modern standards (it required large flat-field corrections). The results are less accurate than those in the bottom panel, but they confirm our composite profile. The best data are shown in the bottom panel. They are remarkably consistent. Except at small and large radii, almost all of the scatter is less than $\pm 0.02 \text{ mag arcsec}^{-2}$. Systematic fitting errors much larger than this imply that a model disagrees with the photometry.

Finally, Figure 5 shows the ellipticity profile. Because of the disk distortion, the apparent ellipticity gets larger as the resolution improves. The VISTA isophote fitting program is especially sensitive to an edge-on embedded disk, so the CFHT and *HST* data show it very strongly. As found already by Scorza & Bender (1995), Figure 5 shows that the embedded disk contributes most at $r \simeq 5''$. Our modeling results are insensitive to the adopted flattening, so we assume that $\epsilon = 0.5$ at all radii.

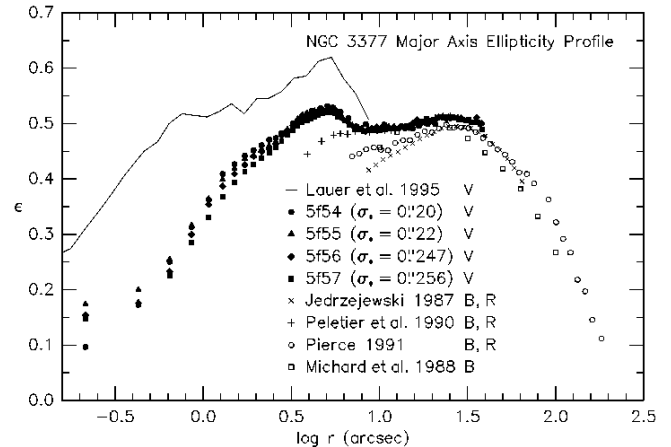


FIG. 5.—Isophote ellipticity $\epsilon = 1 - b/a$ as a function of major-axis radius in NGC 3377 (b/a is isophote axial ratio).

4. ANALYSIS TECHNIQUE

To derive masses and mass-to-light ratios as a function of radius, we need seeing-corrected and unprojected brightnesses, rotation velocities, and velocity dispersions. As in previous papers, we do not try to invent a deconvolution and deprojection technique that is powerful enough to produce unique results. Instead, we convolve models with seeing and compare them to the data. Also, we do not try to prove uniqueness. Rather, we construct fits that bracket the observations in $V(r)$, and $\sigma(r)$. In particular, we find low-mass “error bar” models in which the calculated $V(r)$ and $\sigma(r)$ are too small near the center.

One more piece of machinery is needed. Fourier quotient measurements respond nonlinearly to mixtures of stellar populations with different dispersions. Also, the observed dispersion comes partly from rotational line broadening. Model calculations therefore mimic the construction by seeing and projection of the observed spectra. The first step is to make a library of input spectra suitable for NGC 3377. It consists of the spectrum of the standard star broadened to $\sigma = 60 - 240 \text{ km s}^{-1}$ in steps of 20 km s^{-1} ; for each σ there are entries at $V = -1000$ to 1000 km s^{-1} in steps of 20 km s^{-1} . The library is used to construct synthetic “observed” spectra, as follows. We begin with a trial unprojected rotation curve $V(r)$ and dispersion profile $\sigma(r)$, both assumed to be independent of distance from the equatorial plane. Then for each radius r along the major axis, consider all other pixels at radius \tilde{r}' and depth z' along the line of sight. We calculate the luminosity-weighted projected spectrum at \tilde{r}' . This scatters light into the model pixel by an amount proportional to $I_*(r_*)$, where I_* is a star profile with $\sigma_* = 0''.20$ and $r_* = |\tilde{r}' - r|$.

Here I_* was measured for stars in the bracketing direct images that were taken to check the galaxy centering for spectrum 80f027; they were fitted with a modified Moffat (1969) function to give the PSF used in the analysis,

$$I_*(r_*) = \frac{1}{\left[1 + \left(\frac{r_*}{0''.29701}\right)^{2.68487}\right]^{1.54730}}. \quad (1)$$

The output spectrum is the sum over all scattering pixels of the projected spectra weighted by the product of the projected brightness and the star profile. The pixels used in the calculation are smaller by a factor of 3.5 than the ones in spectrum 80f027 (1 pixel = $0''.043$). The integration is carried out to $r_* = 5\sigma_*$ to include the non-Gaussian wings in the star profile. Finally, the model spectrum is analyzed with the Fourier program. The parameters of the model are then varied until the results fit the kinematics. Uncertainties are estimated by exploring the range of $V(r)$ and $\sigma(r)$ allowed by the data. This technique was developed independently by Kormendy (1988a, b) and by Dressler & Richstone (1988).

The calculations are routine but time-consuming. To keep them manageable, seeing effects are calculated only $|z| = 5''.1$ deep along the line of sight. A separate model run with $\sigma_* = 0''$ does the projection integral for $5''.1 \leq |z| \leq 166''$. We checked that seeing is not important for $|z| > 5''.1$. At each radius in the output image, the two synthetic spectra are sums of 116,040 and 3,740 spectra, respectively. Their sum is the required model spectrum.

Finally, the mass inside r is given by the first velocity moment of the collisionless Boltzmann equation,

$$M(r) = \frac{V^2 r}{G} + \frac{\sigma_r^2 r}{G} \left[-\frac{d \ln \rho}{d \ln r} - \frac{d \ln \sigma_r^2}{d \ln r} - \left(1 - \frac{\sigma_\theta^2}{\sigma_r^2}\right) - \left(1 - \frac{\sigma_\phi^2}{\sigma_r^2}\right) \right]. \quad (2)$$

Here σ_r , σ_θ , and σ_ϕ are the radial and two tangential components of the unprojected velocity dispersion. Also, ρ is the unprojected density of the stars that contribute to the spectra. We assume that M/L_V for these stars is independent of radius; then $d \ln \rho / d \ln r = d \ln I / d \ln r$. Equation (2) is based on the approximations that the mean rotation is circular and that the mass distribution is spherical. We will correct the results for the flattening of the galaxy in § 8.

If M/L_V is nearly constant at large radii and if it rises rapidly toward the center at $r \lesssim 1''$, then there is evidence for a central dark object.

5. VOLUME LUMINOSITY PROFILE

Previous BH papers were based on ground-based measurements of brightness profiles. Consequently it was necessary to model the effects of seeing on $I(r)$ in the same way that we model its effects of V and σ : we constructed a series of analytic approximations to $I(r)$ near the center that bracketed the observed profile after projection and seeing-convolution. This is not necessary for NGC 3377, because *Hubble Space Telescope* (*HST*) measurements of its projected profile (Lauer *et al.* 1995, 1997) have essentially infinite resolution compared to the spectroscopic resolution. We have therefore constructed a composite projected brightness profile from $0''.022$ to $182''$

by using the *HST* profile at $r < 4''$ and the best ground-based measurements in Figure 3 at $r > 4''$. This profile was deprojected and the result was used as the luminosity model in all calculations discussed below. Preliminary results reported earlier (e. g., Kormendy 1992b) were based on analytic luminosity models such as those discussed above; the results did not change significantly when the *HST* profile was adopted because it is almost identical to one of the analytic models.

The mean projected and unprojected major-axis brightness profiles of NGC 3377 are illustrated in Fig. 6.

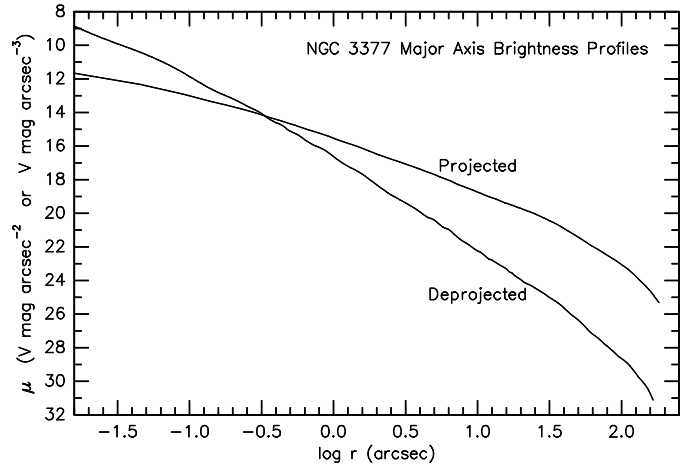


FIG. 6.—Composite *HST* and ground-based major-axis brightness profile of NGC 3377 before and after deprojection.

6. ISOTROPIC KINEMATIC MODELS

We used the machinery of § 4 to find the best-fitting isotropic model and several that bracket the observations. The unprojected model rotation and dispersion profiles are shown in Figure 7, fits to the kinematic data are shown in Figure 8, and the mass-to-light ratio profiles are shown in Figure 9. Figure 10 shows residual mass-to-light ratios after various MDO masses are subtracted. Table 4 lists the model parameters.

Unprojected rotation and dispersion profiles were chosen as in previous papers. Each rotation curve is the sum in quadrature of a Keplerian and three rotation curves for exponential disks (Freeman 1970). This sounds complicated, but we emphasize that these are no more than convenient fitting functions. The total unprojected rotation curves (Fig. 7) are simple: they rise very slowly from large radii toward the center and then either drop to zero, stay constant, or rise steeply inside $1''$. The Keplerian and the central exponential rotation curve are varied to bracket the observed amount of rotation at $r \lesssim 1''$ and hence to see how much central mass is implied by the observations. Two more exponential disk rotation curves are needed to fit the outer rotation curve; the reason is that these are not particularly suitable “basis functions” to fit an almost-flat rotation curve. The present models are slightly more complicated than the ones used in earlier papers because we need to model an almost-flat rotation curve over a larger range in radius. Similarly, the unprojected velocity dispersion is assumed to be the sum in quadrature of a “Keplerian” $\sigma = \sigma_K / r^{1/2}$, r in arcsec, and a constant σ_c . The total V and σ are restricted to be $\geq 111 \text{ km s}^{-1}$ and $\geq 70 \text{ km s}^{-1}$, respectively.

TABLE 4
ISOTROPIC KINEMATIC MODELS

Model	V_K	V_E	r_0	V_E	r_0	V_E	r_0	σ_K	σ_c	$M_{\bullet}^{0.1}$	$M_{\bullet}^{M/L}$	$\langle M/L_V \rangle$
	(km s ⁻¹)	(km s ⁻¹)	(arcsec)	(km s ⁻¹)	(arcsec)	(km s ⁻¹)	(arcsec)	(km s ⁻¹)	(km s ⁻¹)	(10 ⁸ M _⊙)	(10 ⁸ M _⊙)	(M _⊙ /L _{V⊙})
(1)	(2)	(3)	(4)	(5)	(6)	(7)	(8)	(9)	(10)	(11)	(12)	(13)
1	122	103	0.30	112	1.1	103	7.0	102	45	3.0	3.6	2.3
2	122	103	0.30	112	1.1	103	7.0	99	45	1.7	2.8	2.4
3	0	172	0.30	99	1.2	105	7.0	96	45	1.4	2.4	2.5
4	0	156	0.45	86	1.2	105	7.0	90	45	1.3	1.8	2.5
5	0	144	0.60	80	1.2	105	7.0	85	45	1.3	1.2	2.6
6	45	175	0.25	102	1.2	105	7.0	96	45	1.6	2.7	2.5
7	55	159	0.35	93	1.2	105	7.0	96	45	1.7	2.6	2.5
8	63	155	0.47	74	1.5	104	7.0	96	45	1.8	2.4	2.5
9	71	154	0.60	54	1.8	103	7.0	96	45	1.9	2.3	2.5
1m	112	95	0.30	103	1.1	95	7.0	105	45	2.7	3.3	2.3
2m	112	95	0.30	103	1.1	95	7.0	104	45	1.6	2.7	2.4
3m	0	158	0.30	91	1.2	97	7.0	98	45	1.4	2.3	2.4
4m	0	144	0.45	79	1.2	97	7.0	92	45	1.3	1.7	2.4
5m	0	133	0.60	74	1.2	97	7.0	87	45	1.3	1.1	2.5

NOTES. – Column (1), model number (Fig. 7 – 15). Columns (2) – (8), rotation curve parameters. A rotation curve consists of the sum in quadrature of a Keplerian with velocity V_K at 1'' (Column 2) and three exponential disk rotation curves, each with a maximum velocity V_E and a scale length r_0 (Columns 3 – 8). Similarly, the total velocity dispersion σ is the sum in quadrature of a “Keplerian” with dispersion σ_K at 1'' (Column 9) and a constant σ_c (Column 10). The minimum total velocity and velocity dispersion allowed are 111 km s⁻¹ and 70 km s⁻¹, respectively. In models 2 and 2m, $V \leq 184$ km s⁻¹ and $V \leq 169$ km s⁻¹, respectively. Column (11), total mass inside 0''.1. Column (12), central dark mass estimated by requiring that the MDO-subtracted mass-to-light ratio at $r \lesssim 25''$ (Column 13) be as nearly constant as possible. Except for $M_{\bullet}^{0.1}$, masses and mass-to-light ratios are corrected for the E5 shape of the galaxy (see § 8). The distance to NGC 3377 is assumed to be 9.9 Mpc.

The best-fitting model, number 3, is a good fit to both the rotation and the dispersion profiles (Fig. 8). Its dispersion gradient is not quite steep enough to be a perfect fit to the low observed $\sigma \simeq 100$ km s⁻¹ at 1'', and similarly, the rotation curve rises to a slightly sharper peak an 0''.9. These features in the data are probably due to the embedded disk structure (Scorza & Bender 1995). But the slope of the inner rotation curve is fitted essentially perfectly. If we slightly underestimate the slope in $\sigma(r)$, we only underestimate M_{\bullet} . Compared to model 3, models 2 and 1 have progressively more rotation and steeper dispersion gradients near the center. Model 2 is a reasonable “error bar”, while model 1 is clearly excluded by the data. Similarly, models 4 and 5 have too little rotation and dispersion gradient near the center; model 4 is a reasonable “error bar”, while model 5 is clearly excluded.

Figure 9 shows the corresponding mass-to-light ratios. It is interesting and reassuring that all models imply constant mass-to-light ratios $M/L_V \simeq 2.6$ to 3 between $r \simeq 2''$ and 35''. This means that the inner part of the galaxy is dominated by an old stellar population, with no significant contribution from halo dark matter. The same is true in NGC 3115 (Kormendy & Richstone 1992) and in NGC 4594 (Kormendy & Westpfahl 1989). In all three galaxies, the M/L profile at large radii is simple and requires no unseen mass other than that normally associated with stars. This is a useful result in its own right. Since the volume brightness changes by a factor of ~ 630 over this radius range, and since the modeling machinery allows M/L_V to vary as much as it likes, the constancy of M/L_V

is a good sign that the machinery is working correctly.

In contrast, M/L_V increases at $r < 2''$ by a factor of at least 4. The absolute values to which M/L_V rises are not larger than we see in more luminous ellipticals. Also, the rise is important only at small radii. Finally, it is possible to make anisotropic, three-integral maximum entropy models (Richstone *et al.* 1998a) that fit the data without an MDO. Therefore this is a weaker MDO detection than those in the Galaxy, M31, M32, and NGC 3115 (KR95).

As in previous papers, we derive two estimates of the mass of the central dark object (Table 4). First, $M_{\bullet}^{0.1}$ is the total mass interior to $r = 0''.1$. Unlike estimates that depend on the mass distribution at $r \gtrsim 0''.5$, this value is not corrected for the flattening of the galaxy, because the potential near the center is almost spherical. If the stellar mass-to-light ratio is nearly constant with radius as suggested by the lack of strong line-strength gradients, then Fig. 9 implies that essentially all of the mass inside 0''.1 radius is dark. However, $M_{\bullet}^{0.1}$ is very sensitive to the effects of projection and seeing. Also, when it is subtracted from the mass distribution, a mass-to-light ratio gradient remains. A second estimate is therefore derived by requiring that the residual $M/L_V(r)$ be as nearly constant as possible after a central point mass $M_{\bullet}^{M/L}$ is subtracted. Figure 10 shows the residual $M/L_V(r)$. It varies slightly with radius; the MDO mass is therefore uncertain by about $\pm 0.4 \times 10^8 M_{\odot}$ (slightly more for model 1 and less for model 5). The adopted mass for model 3 is $M_{\bullet}^{M/L} = 2.4 \times 10^8 M_{\odot}$. The “error bar” models 2 and 4 imply that the uncertainty is about $\pm 0.7 \times 10^8 M_{\odot}$.

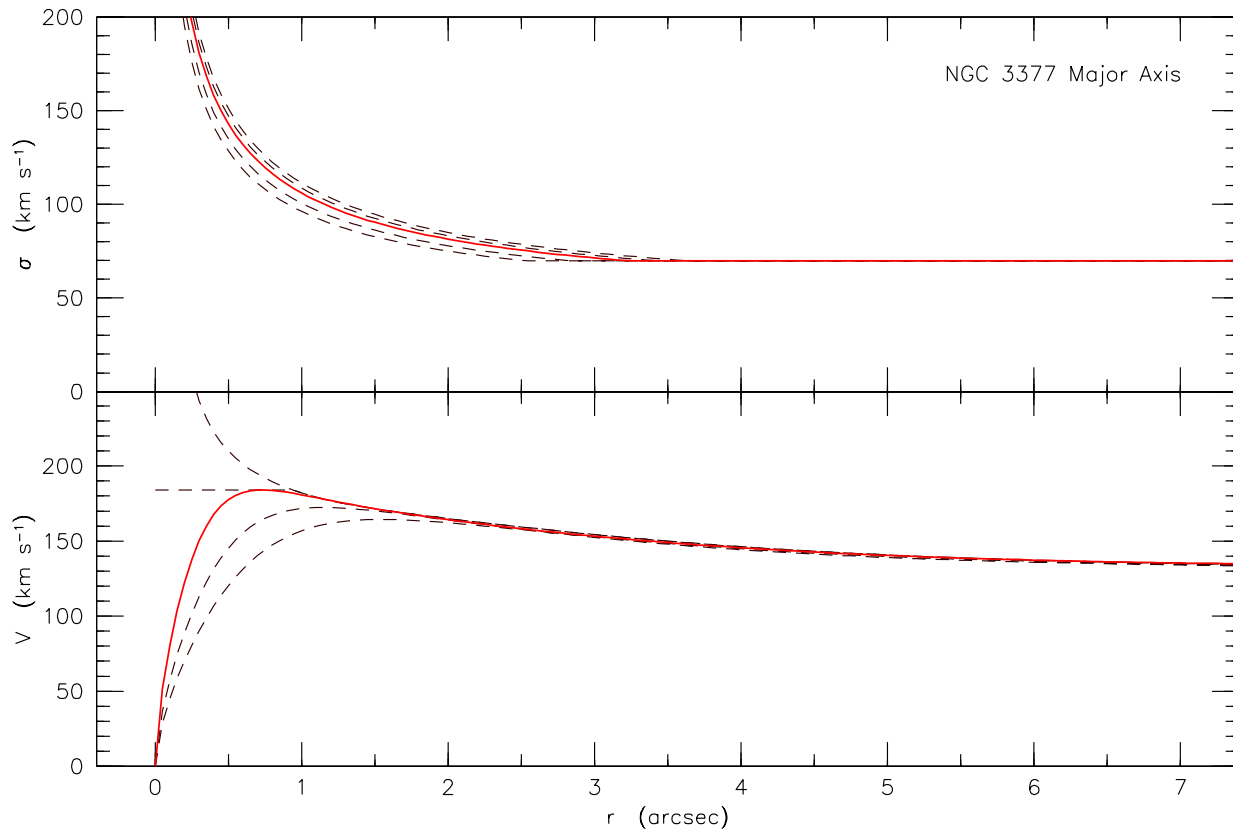


FIG. 7.—Intrinsic (i. e., not projected or seeing-convolved) rotation and dispersion profiles for kinematic models 1 – 5 in Table 4.

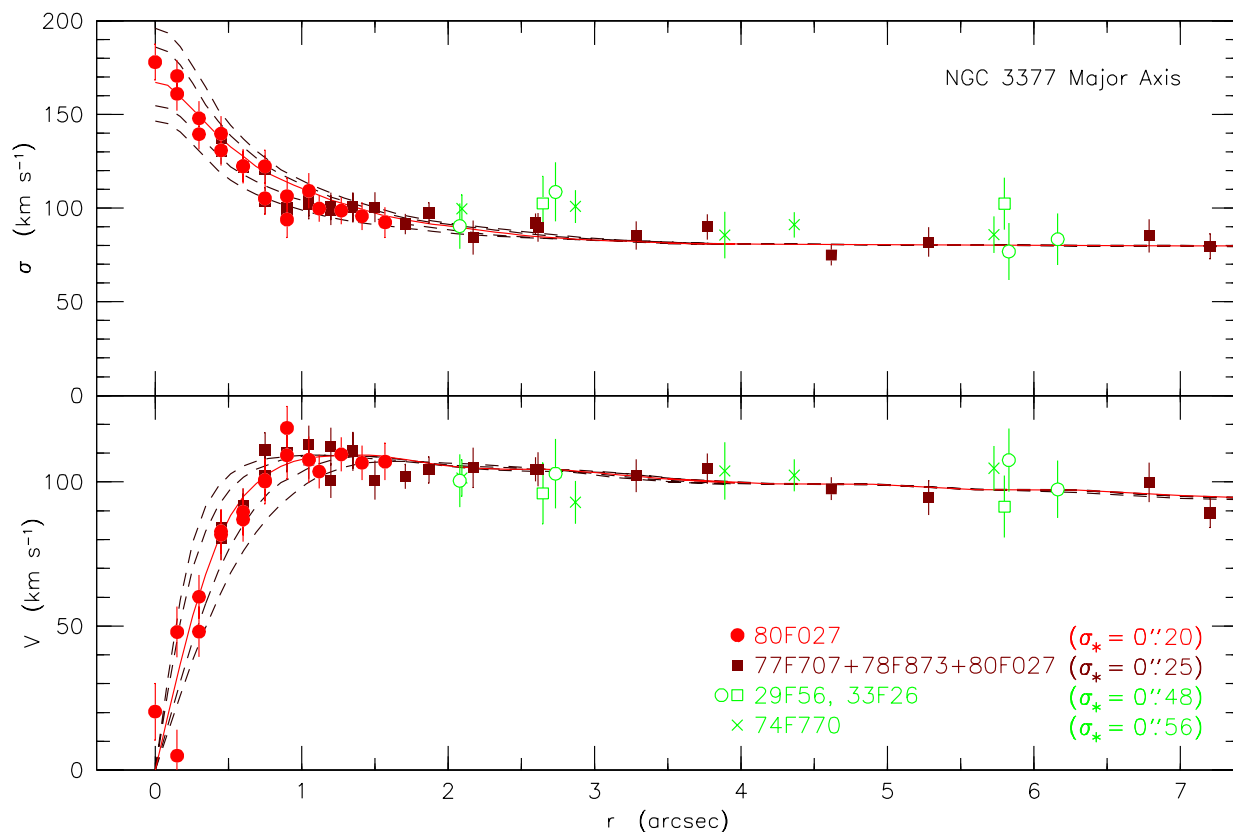


FIG. 8.—Models 1 – 5 (top to bottom at $0''.4$) fitted to the major-axis kinematic data. Here the models have been projected and convolved with seeing as discussed in §4. Only the high-resolution data are plotted inside $r = 2''$.

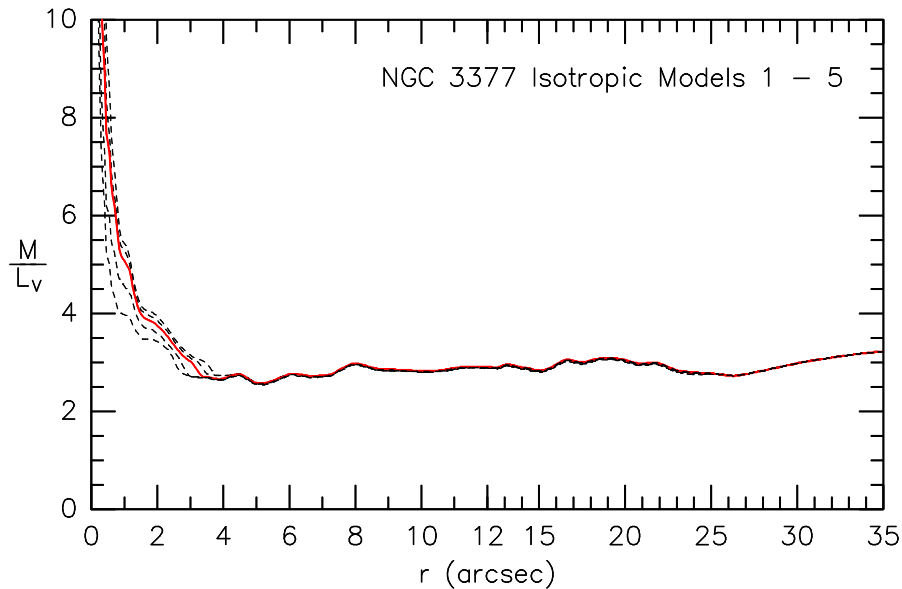


FIG. 9.—Mass-to-light ratio M/L_V (solar units) as a function of radius for models 1 – 5, corrected for the E5 shape of the galaxy.

Averaging this result with $M_{\bullet}^{0.1}$, we arrive at our final estimate for the MDO mass given by models 1 – 5, $M_{\bullet} = (1.9 \pm 0.8) \times 10^8 M_{\odot}$. The errors are not Gaussian: a range of M_{\bullet} values is allowed because of parameter coupling in the models, but outside the above range, masses become rapidly excluded by the present machinery.

Model 3 fits the data and implies that NGC 3377 contains an MDO, but it has a shortcoming. The rotation velocity decreases to zero at the center. This is not impossible in principle – the BH detection comes mostly from the dispersion gradient – but it is not the natural expectation. It is important to note that we are just measuring masses, like when we use an embedded HI disk to measure the mass of a galaxy, but with the added complication of a non-zero velocity dispersion. We are not making self-consistent dynamical models. So we may be allowing some freedom in the tradeoff between V and σ that the galaxy does not have. The results of such models have proved to be very reliable in the past (see, e.g., Kormendy *et al.* 1996a, b and van der Marel *et al.* 1997a, b, which compare *HST* results on NGC 3115, NGC 4594, and M32 with BH results from papers using techniques like ours). Nevertheless, the tradeoff between V and σ deserves further exploration.

We have therefore constructed a more closely spaced series of models that have various small amounts of Keplerian rotation curve near the center. These are models 6 – 9 in Table 4; they are illustrated in Figures 11 – 13. Models 7 and 8 are good fits to the data. In fact, they are better fits than model 3, because the extra rotational line broadening allows a better fit of the central velocity dispersion. Models 6 and 9 are error bars to $V(r)$, although they are not excluded by the data. Their rotation curves are slightly more complicated than those of models 1 – 5 (see Fig. 11). Other, similar models are possible. But these, too, have steeply rising mass-to-light ratio profiles near the center (Fig. 13), and in these cases, the central dark mass is implied by both V and σ .

Together, models 1 – 9 show that the detection of a central dark object in NGC 3377 is very robust, within the assumption that the velocity distribution is isotropic. The

implied mass is $M_{\bullet} = (1.9 \pm 0.8) \times 10^8 M_{\odot}$. It requires two small corrections. It already contains a correction for the flattening of the galaxy; this is discussed in § 8. Also, in § 7, we correct for the fact that we fit Gaussians to the line-of-sight velocity distributions instead of measuring moments as required by Equation (2).

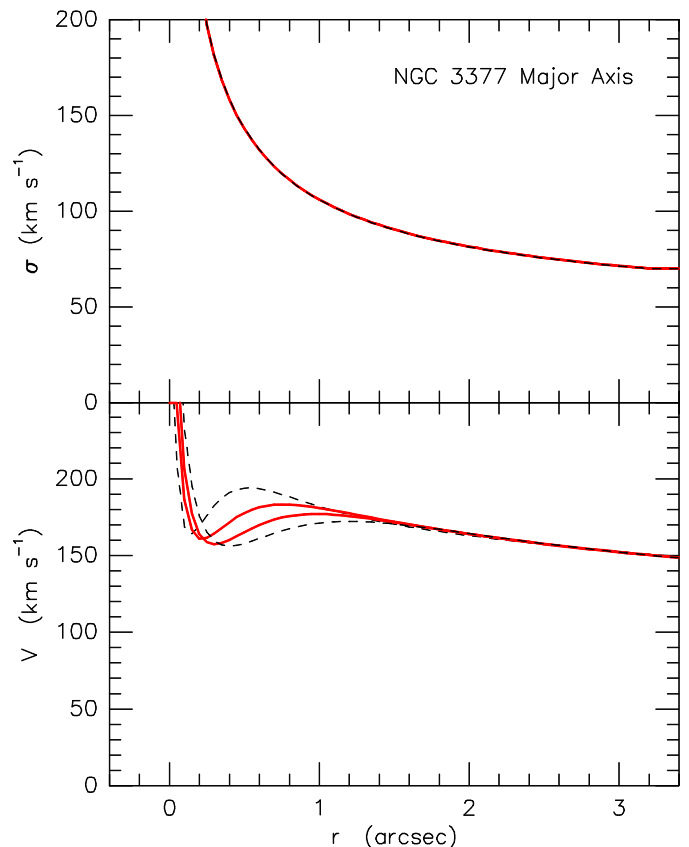


FIG. 11.—Intrinsic (i. e., not projected or seeing-convolved) rotation and dispersion profiles for kinematic models 6 – 9.

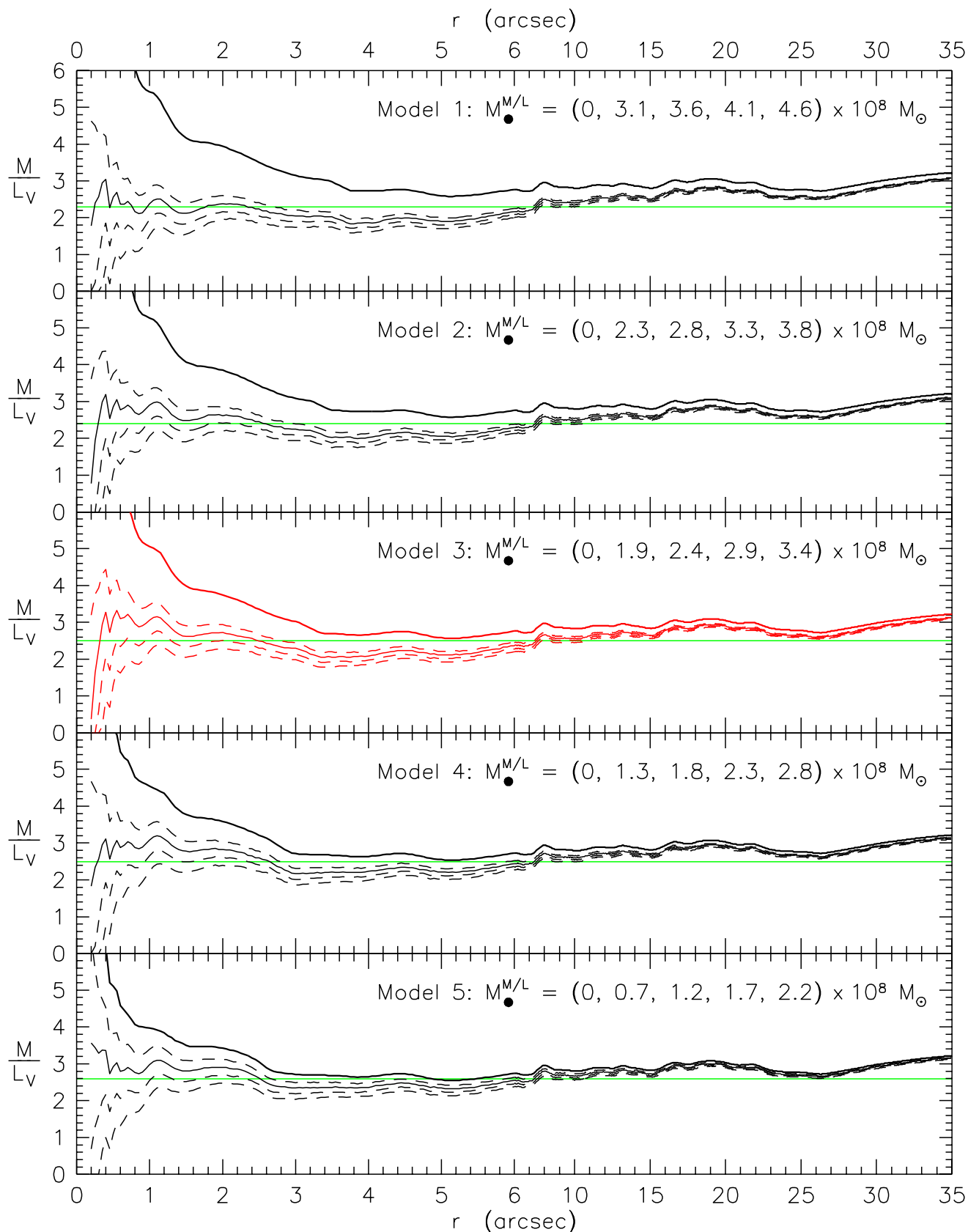


FIG. 10.—Mass-to-light ratio M/L_V as a function of radius for models 1 – 5 before (heavy solid lines) and after (light lines) subtraction of the MDO masses listed in the keys. At $r < 0''.2$, the curves get very noisy and so are not plotted. For each model, residuals are shown for four values of $M_{\bullet}^{M/L}$; the second-smallest, which corresponds to the light solid line, is the adopted value. The others (dashed lines) illustrate the uncertainty that results from the fact that M/L_V is not exactly constant with radius. The horizontal straight line in each panel is the adopted mean stellar mass-to-light ratio. All mass-to-light ratios are corrected for the E5 shape of the galaxy.

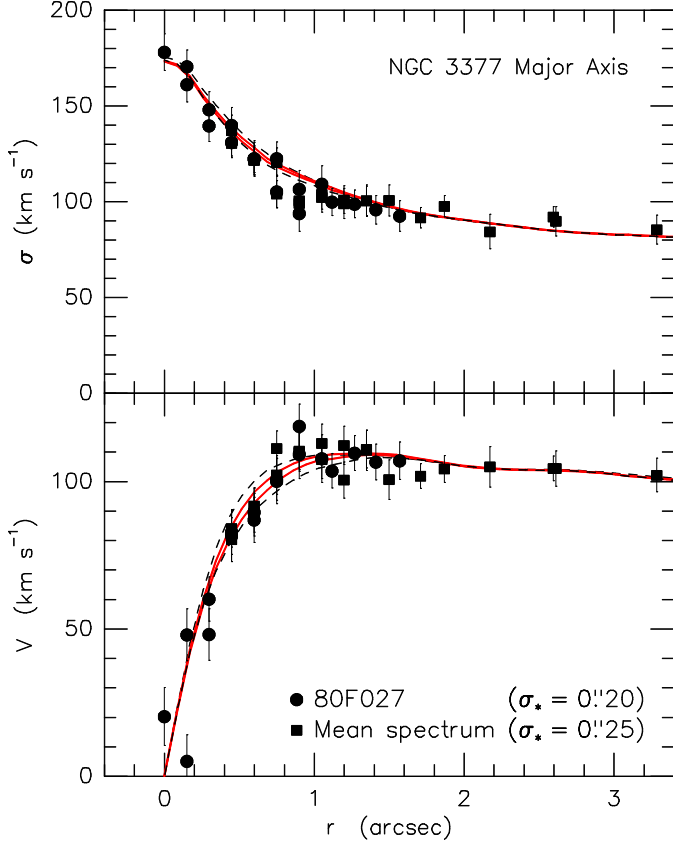


FIG. 12.—Models 6 – 9 (top to bottom at 0''6) fitted to the major-axis kinematic data. Here the models have been projected and convolved with seeing. Only the high-resolution data are plotted.

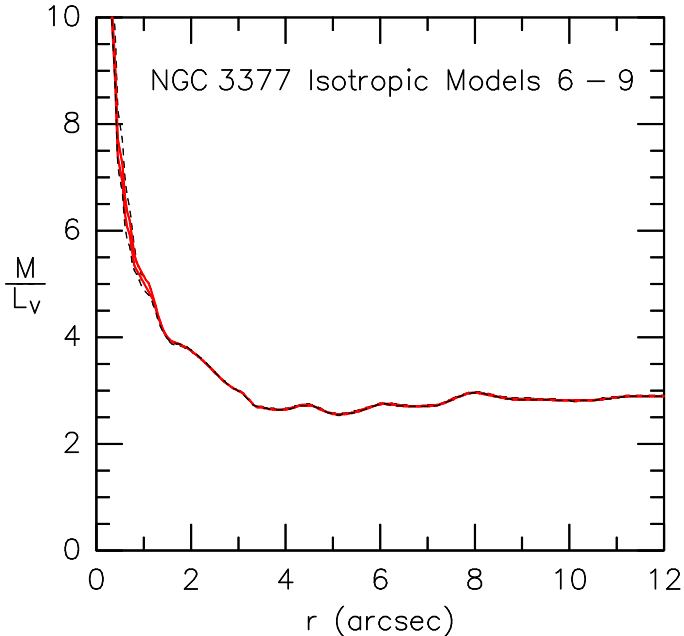


FIG. 13.—Mass-to-light ratio M/L_V (solar units) as a function of radius for models 6 – 9, corrected for the E5 flattening of NGC 3377 as discussed in § 8.

7. LINE-OF-SIGHT VELOCITY DISTRIBUTIONS

The quantities V and σ in Equation (2) are moments of the line-of-sight velocity distribution (LOSVD). In real life, moments cannot be measured, because they are sensitive to small numbers of stars that are far from the mean velocity and hence out in the (unknown) continuum. In § 2, we derived velocities and velocity dispersions by fitting Gaussians to the line profiles. Several authors have pointed out that the derivation of $M(r)$ can suffer systematic errors if such measurements are substituted for moments (van der Marel & Franx 1993; van der Marel *et al.* 1994a, b; Bender *et al.* 1994). However, KR95 (see p. 598 – 599) point out that the moment $V(r)$ is proportional to the Gaussian fit $V(r)$, so the main effect is to lower the global (i. e., bulge) mass-to-light ratio slightly; the strength of the BH case is almost unchanged. Since many BH papers are based on Gaussian fit V and σ values, it is useful to illustrate this point for at least one galaxy. Therefore we investigate here how LOSVD asymmetries affect the conclusions of § 6.

We measured non-parametric LOSVDs using the Fourier Correlation Quotient method (FCQ, Bender 1990). To extract higher-order information on the LOSVD shapes, we fitted them with a Gaussian plus third- and fourth-order Gauss-Hermite polynomials H_3 and H_4 (van der Marel & Franx 1993, Gerhard 1993):

$$\text{LOSVD}(v) = \frac{\gamma}{\sqrt{2\pi\sigma^2}} e^{-\frac{(v-V)^2}{2\sigma^2}} \cdot \left[1 + h_3 H_3\left(\frac{v-V}{\sigma}\right) + h_4 H_4\left(\frac{v-V}{\sigma}\right) \right]. \quad (3)$$

The coefficients h_3 and h_4 parametrize the lowest-order asymmetric and symmetric deviations from Gaussian line profiles. Positive h_4 implies that the line profile is more triangular than Gaussian; i. e., it is more strongly peaked and has more extended wings than the best-fitting Gaussian. Negative h_4 parametrizes deviations toward rectangular line profiles. The h_4 amplitudes are generally small in ellipticals, with values less than a few percent (Bender *et al.* 1994). This is also the case in NGC 3377: $h_4 \simeq 0$ at $r \leq 6''$. The FCQ results are shown in Fig. 14.

The h_3 amplitude can reach values of ± 0.15 ; it couples with rotation as $h_3 \simeq -0.1 V/\sigma$ (Bender *et al.* 1994). In NGC 3377, $h_3 = -0.09 V/\sigma$ with no significant deviations (Fig. 14). Therefore there are more stars on the retrograde (systemic-velocity) side of the LOSVD than on the prograde side. Such behavior is natural for rotating stellar systems (see the above references); it is especially expected when there is a disk, rapidly-rotating structure embedded in a more nearly spherical and slowly-rotating body (Scorza & Bender 1995).

Having measured h_3 and h_4 profiles, we can derive more realistic estimates of the velocity moments than we got from Gaussian fits alone. For the case $h_4 \simeq 0$ and $-0.15 < h_3 < 0$, Bender *et al.* (1994, see Fig. 3) find that

$$\frac{V_{\text{mom}} - V_{\text{fit}}}{\sigma_{\text{fit}}} = -1.0 |h_3|^{0.83}; \quad (4)$$

$$\frac{\sigma_{\text{mom}} - \sigma_{\text{fit}}}{\sigma_{\text{fit}}} = 4.7 |h_3|^{2.4}. \quad (5)$$

Here V_{mom} and σ_{mom} are the approximate true moments, and V_{fit} and σ_{fit} are derived by fitting Equation (3) to

the LOSVDs. Moments derived in this way are illustrated in Figure 14, together with the velocities and velocity dispersions given by the Fourier Quotient and Fourier Correlation Quotient methods. The velocity dispersions are virtually identical for all three procedures, but the velocities differ by up to 15%. As expected for negative h_3 , the velocity moments are smaller than both the FQ and FCQ fitted values. However, the FQ values are between the FCQ and moment velocities. Therefore Gaussian fits give velocities that are closer to the true moments than higher-order fits incorporating h_3 and h_4 .

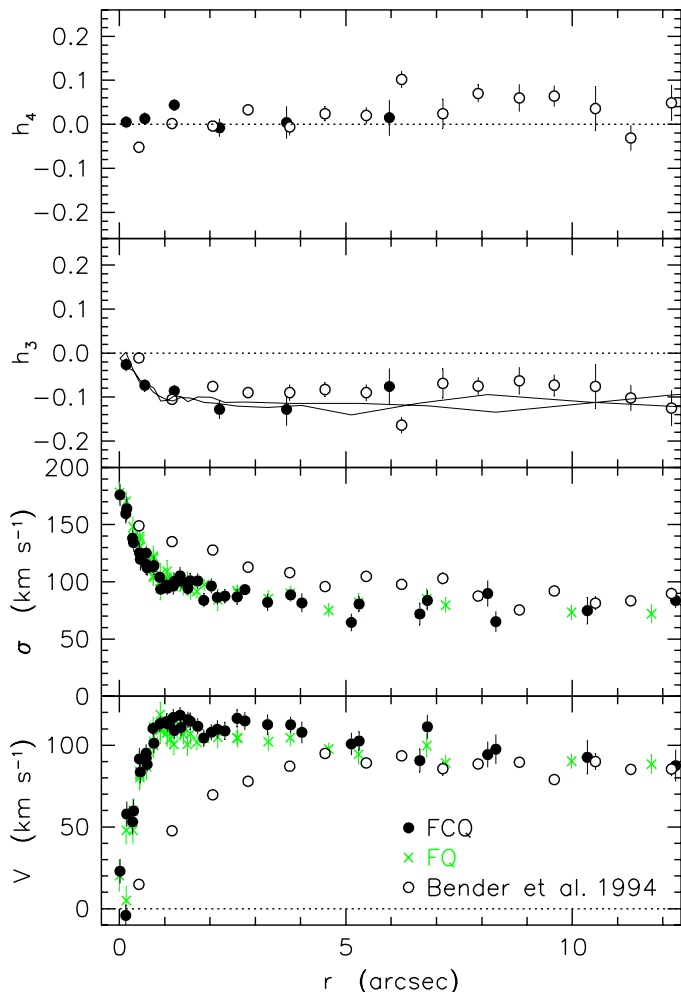


FIG. 14.—Fourier Correlation Quotient measurements of V , σ , h_3 , and h_4 along the major axis of NGC 3377. The FQ results are shown for comparison. In the h_3 panel, the lines show $h_3 = -0.09 V/\sigma$ calculated from the filled circles in the bottom two panels.

How do these results affect the mass measurements in this and previous BH papers? Figure 14 confirms the remark in KR95 that the velocity moments are smaller than the FQ velocities by a scale factor that is almost independent of radius. Models 1m – 5m (Table 4) are models 1 – 5 recalculated with velocities scaled down by a factor of 0.92. They fit the moment data in Figure 14 in the same way that models 1 – 5 fit the FQ data in Figure 8. Model 3m is a good fit; model 4m provides a low- M_\bullet error bar, and model 5m clearly does not fit the data. Models 1m and 2m similarly provide high- M_\bullet error bars.

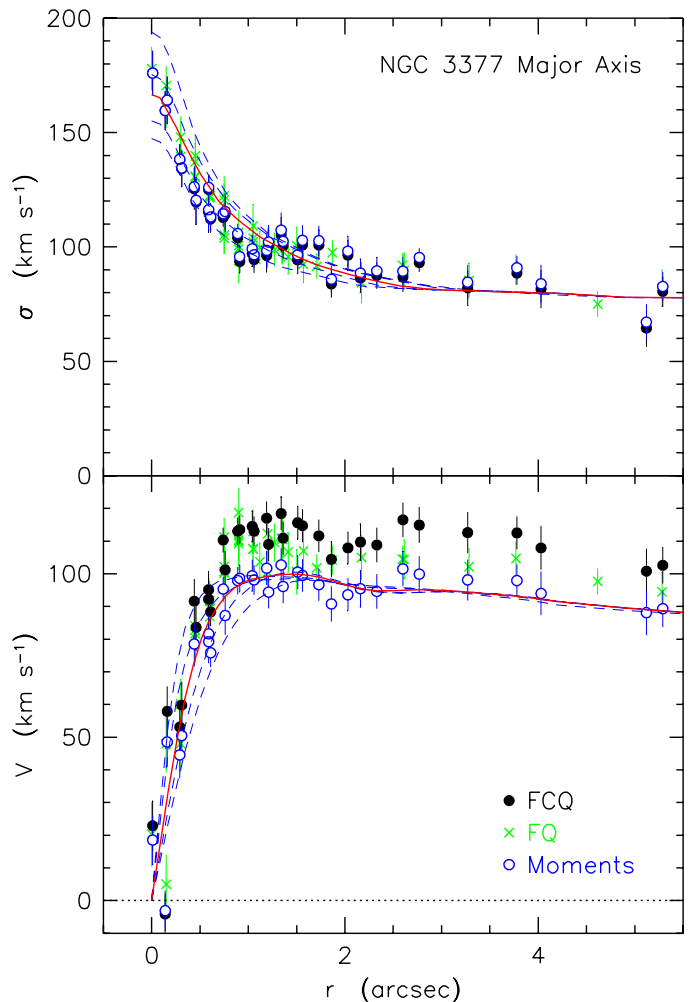


FIG. 15.—Comparison of Fourier Quotient measurements, Fourier Correlation Quotient measurements, and approximate velocity moments calculated from the FCQ measurements using Equations 4 and 5. The lines show models 1m – 5m, i. e., models 1 – 5 with velocities scaled down by a factor of 0.92.

Figure 16 shows the mass-to-light ratio profiles for models 1m – 5m. As expected, they are similar in shape to those in Fig. 9; i. e., M/L_V still climbs quickly at $r \lesssim 2''$. This means that the strength of the BH case is essentially unchanged. But the overall mass scale is slightly smaller. The factor is not as extreme as 0.92^2 , because $\sigma(r)$ must be made steeper to preserve a good fit to the data now that rotational line broadening is reduced. The BH masses and mass-to-light ratios are given for models 1m – 5m in Table 4. We find that $M_\bullet = (1.8 \pm 0.8) \times 10^8 M_\odot$.

Note that models 1m – 5m are not attempts to fit the full LOSVDs of NGC 3377, i. e., they are not intended to model the complete dynamical behavior of the galaxy. They have essentially Gaussian LOSVDs; this is why they do not themselves require a correction from Gaussian fit to moment V and σ values. We emphasize that the purpose of this paper is only to measure the mass distribution well enough to search for a BH. With models 1m – 5m, we have corrected our measurements of $M(r)$ and M_\bullet for the most important effects of LOSVD asymmetries. As expected, the corrections are small. Similar conclusions apply to past BH papers based on FQ measurements: the errors made by neglecting h_3 and h_4 are small compared to other uncertainties in the analysis. This is especially true

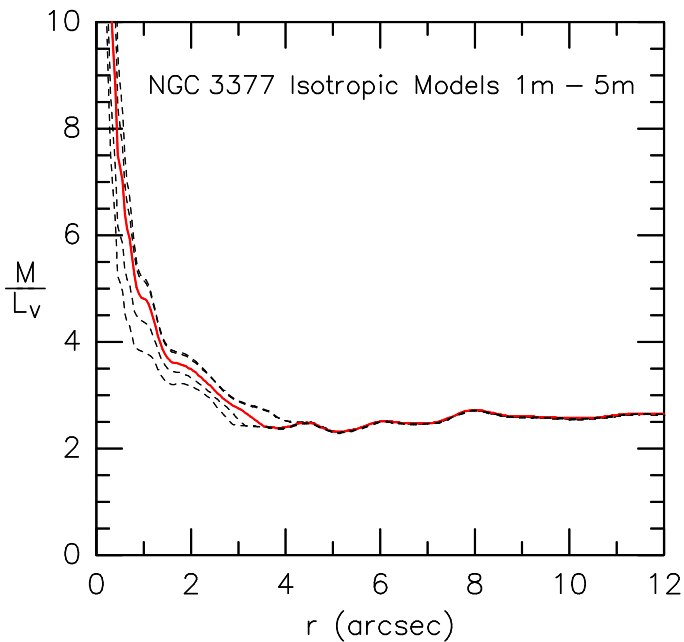


FIG. 16.—Mass-to-light ratio M/L_V (solar units) as a function of radius for models 1m – 5m, corrected for the E5 flattening of NGC 3377 as discussed in §8.

when bulge-subtracted spectra were analyzed (Kormendy 1988b,c), since bulge subtraction removes most of the LOSVD asymmetries (Kormendy 1994).

8. DISCUSSION

Isotropic models imply that NGC 3377 contains a central dark object, probably a BH, of mass $M_\bullet \sim 2 \times 10^8 M_\odot$. The BH mass and stellar mass-to-light ratio require one more correction. While the fits of the kinematic models to the observations were correctly based on an E5 light distribution, the $M(r)$ and $L(r)$ calculations were based on the approximation that the galaxy is spherical. For any test particle at radius r along the major axis, the observed velocities imply less mass in a flattened galaxy because stars are on average closer to the test particle than we assumed. Binney & Tremaine (1987) give the required correction in their Fig. 2-12. This is for a modified Hubble density distribution, which is not a bad approximation here. The E0 and E5 rotation curves are proportional to each other; the flattening correction to $M(r)$ is a factor of 0.80. This is approximate, because we assume that the mass distribution is E5 everywhere, whereas in reality, it gets rounder as $r \rightarrow 0$ because of the BH. Nevertheless, the correction should be accurate enough so that other uncertainties dominate. Similarly, the correction to $L(r)$ is a factor of 0.5. Therefore we correct M_\bullet by a factor of 0.80 and $M/L(r)$ by a factor of $0.80/0.5 = 1.61$. Table 4 and Figures 9, 13, and 16 include these corrections.

We conclude that isotropic kinematic models imply that NGC 3377 contains a central dark object of mass $M_\bullet = (1.8 \pm 0.8) \times 10^8 M_\odot$. The stellar mass-to-light ratio $M/L_V = 2.4 \pm 0.2$ is smaller than normal for an elliptical of absolute magnitude $M_B = -18.8$ (e. g., Kormendy 1987b, Fig. 3; note that this is based on a Hubble constant of $50 \text{ km s}^{-1} \text{ Mpc}^{-1}$). The BH mass supports the emerging correlation between bulge luminosity and M_\bullet (Fig. 17; Kormendy *et al.* 1997; KR95; Kormendy 1993).

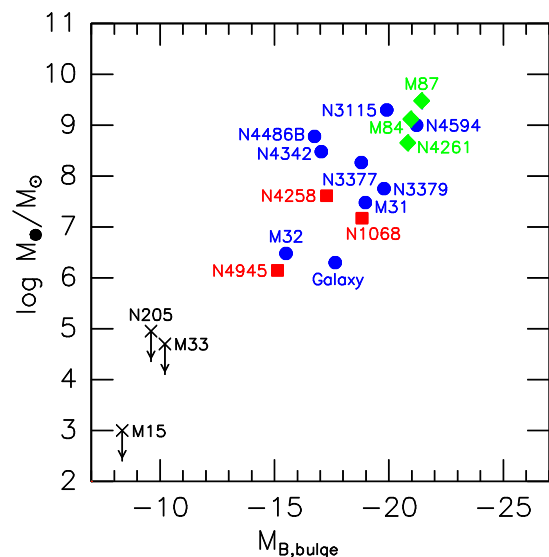


FIG. 17.—BH mass as a function of bulge absolute magnitude, from Kormendy *et al.* (1997) but with M 84 (Bower *et al.* 1998; Green 1997) and NGC 4342 (van den Bosch & Jaffe 1997; Cretton & van den Bosch 1998) added and with NGC 3377 updated. Circles, diamonds, and squares show objects with stellar-dynamical, ionized gas dynamical, and maser evidence for BHs, respectively. Upper limits on M_\bullet are plotted as crosses. The correlation may be only the upper envelope of a distribution that extends to smaller M_\bullet .

Our detection of an MDO in NGC 3377 is not quite definitive, because anisotropic, three-integral maximum entropy models (Richstone *et al.* 1998a) can fit our data without a BH (Richstone *et al.* 1998b). However, several arguments suggest that NGC 3377 is not likely to be very radially anisotropic. To explain the data without a BH requires that $\sigma_r \gg \sigma_\phi$ and σ_θ . But NGC 3377 contains an embedded nuclear disk (Scorza & Bender 1995). Our understanding of how these form – gas dissipation and star formation – would not tend to make σ_r very large compared to σ_ϕ and σ_θ . In fact, van der Marel *et al.* (1997b) conclude that valid models of M 32, whose kinematics are similar to those of NGC 3377, “are all dominated by azimuthal motion at most radii” (their Fig. 10). Also, NGC 3377 rotates rapidly enough to be near the “oblate line” in the well known $V/\sigma - \epsilon$ diagram (Illingworth 1977; Binney 1978, 1980, 1981, 1982; Binney & Tremaine 1987; $\epsilon =$ ellipticity and $V/\sigma =$ ratio of the maximum rotation velocity to a mean velocity dispersion near the center). The oblate line, $V/\sigma \simeq [\epsilon/(1 - \epsilon)]^{1/2}$ (Kormendy 1982), describes oblate spheroids that are isotropic and flattened only by rotation. This is a direct constraint only on $\sigma_z/(\sigma_r^2 + \sigma_\phi^2)^{1/2}$, but rapidly rotating ellipticals have generally turned out to be less anisotropic than slowly rotating ellipticals. Finally, isotropic model measurements of M_\bullet have turned out to be close to correct when anisotropic models were constructed (see KR95 for a review). So it is likely that our measurement of M_\bullet is reasonably accurate. Nevertheless, it will be important to see whether higher-resolution observations confirm our MDO detection.

This work is in progress: Richstone *et al.* (1998b) have obtained *HST* FOS spectroscopy of NGC 3377. Their three-integral maximum entropy models of NGC 3377 show conclusively that it contains a central dark object of mass $M_\bullet \simeq 10^8 M_\odot$.

JK thanks the staff of the Canada-France-Hawaii Telescope for their support of the observing runs. He is especially grateful to D. Salmon for his care in setting up the f/4 module of the Herzberg Spectrograph. JK is also grateful to N. Trentham for his assistance during Run 3. We thank G. Bower, R. Green, and F. van den Bosch for allowing us to include their M_{\bullet} measurements

in Fig. 17 before publication. We also thank the referee, R. van der Marel, for his helpful comments. JK and AE were supported in part by NSF grants AST-8915021 and AST-9219221. RB's work was supported by Sonderforschungsbereich 375 of the German Science Foundation and by the Max-Planck-Gesellschaft.

REFERENCES

- Bacon, R., Emsellem, E., Monnet, G., & Nieto, J. L. 1994, *A&A*, 281, 691
- Bender, R. 1988, *A&A*, 193, L7
- Bender, R. 1990, *A&A*, 229, 441
- Bender, R., Döbereiner, S., & Möllenhoff, C. 1988, *A&AS*, 74, 385
- Bender, R., Kormendy, J., & Dehnen, W. 1996, *ApJ*, 464, L123
- Bender, R., Saglia, R. P., & Gerhard, O. E. 1994, *MNRAS*, 269, 785
- Bender, R., Surma, P., Döbereiner, S., Möllenhoff, C., & Madejsky, R. 1989, *A&A*, 217, 35
- Binney, J. 1978, *MNRAS*, 183, 501
- Binney, J. 1980, *MNRAS*, 190, 421
- Binney, J. 1981, in *The Structure and Evolution of Normal Galaxies*, ed. S. M. Fall & D. Lynden-Bell (Cambridge: Cambridge Univ. Press), 55
- Binney, J. 1982, in *Morphology and Dynamics of Galaxies, Twelfth Advanced Course of the Swiss Society of Astronomy and Astrophysics*, ed. L. Martinet & M. Mayor (Sauverny: Geneva Observatory), 1
- Binney, J., & de Vaucouleurs, G. 1981, *MNRAS*, 194, 679
- Binney, J., & Tremaine, S. 1987, *Galactic Dynamics* (Princeton: Princeton Univ. Press)
- Bower, G., *et al.* 1998, *ApJL*, in press
- Burstein, D., & Heiles, C. 1984, *ApJS*, 54, 33
- Caldwell, N. 1983, *ApJ*, 268, 90
- Carter, D. 1987, *ApJ*, 312, 514
- Carter, D., & Jenkins, C. R. 1993, *MNRAS*, 263, 1049
- Cretton, N., & van den Bosch, F. C. 1998, in preparation
- Davies, R. L., Efstathiou, G., Fall, S. M., Illingworth, G., & Schechter, P. L. 1983, *ApJ*, 266, 41
- Dehnen, W. 1995, *MNRAS*, 274, 919
- de Vaucouleurs, G. 1948, *Ann. d'Ap.*, 11, 267
- Djorgovski, S. B. 1985, PhD Thesis, University of California at Berkeley
- Dressler, A. 1984, *ApJ*, 286, 97
- Dressler, A., & Richstone, D. O. 1988, *ApJ*, 324, 701
- Emsellem, E., Monnet, G., Bacon, R., & Nieto, J.-L. 1994, *A&A*, 285, 739
- Faber, S. M., *et al.* 1997, *AJ*, 114, 1771
- Ferrarese, L., Ford, H. C., & Jaffe, W. 1996, *ApJ*, 470, 444
- Franx, M., Illingworth, G., & de Zeeuw, T. 1991, *ApJ*, 383, 112
- Freeman, K. C. 1970, *ApJ*, 160, 811
- Gerhard, O. E. 1993, *MNRAS*, 265, 213
- Green, R. F. 1997, private communication
- Harms, R. J., *et al.* 1994, *ApJ*, 435, L35
- Illingworth, G. 1977, *ApJ*, 218, L43
- Jedrzejewski, R. I. 1987, *MNRAS*, 226, 747
- Kent, S. M. 1990, in *The Evolution of the Universe of Galaxies*, ed. R. G. Kron (San Francisco: ASP), 109
- Kormendy, J. 1982, in *Morphology and Dynamics of Galaxies, Twelfth Advanced Course of the Swiss Society of Astronomy and Astrophysics*, ed. L. Martinet and M. Mayor (Sauverny: Geneva Obs.), 113
- Kormendy, J. 1985, *ApJ*, 295, 73
- Kormendy, J. 1987a, in *IAU Symposium 127, Structure and Dynamics of Elliptical Galaxies*, ed. T. de Zeeuw (Dordrecht: Reidel), 17
- Kormendy, J. 1987b, in *Nearly Normal Galaxies: From the Planck Time to the Present*, ed. S. M. Faber (New York: Springer-Verlag), 163
- Kormendy, J. 1988a, in *Supermassive Black Holes*, ed. M. Kafatos (Cambridge: Cambridge Univ. Press), 98
- Kormendy, J. 1988b, *ApJ*, 325, 128
- Kormendy, J. 1988c, *ApJ*, 335, 40
- Kormendy, J. 1992a, in *Testing the AGN Paradigm*, ed. S. S. Holt, S. G. Neff, & C. M. Urry (New York: American Institute of Physics), 23
- Kormendy, J. 1992b, in *High Energy Neutrino Astrophysics*, ed. V. J. Stenger, J. G. Learned, S. Pakvasa, & X. Tata (Singapore: World Scientific), 196
- Kormendy, J. 1993, in *The Nearest Active Galaxies*, ed. J. Beckman, L. Colina & H. Netzer (Madrid: Consejo Superior de Investigaciones Científicas), 197
- Kormendy, J. 1994, in *The Nuclei of Normal Galaxies: Lessons From The Galactic Center*, ed. R. Genzel & A. I. Harris (Dordrecht: Kluwer), 379
- Kormendy, J., *et al.* 1996a, *ApJ*, 459, L57
- Kormendy, J., *et al.* 1996b, *ApJ*, 473, L91
- Kormendy, J., *et al.* 1997, *ApJ*, 482, L139
- Kormendy, J., & Bender, R. 1996, *ApJ*, 464, L119
- Kormendy, J., & Illingworth, G. 1982, *ApJ*, 256, 460
- Kormendy, J., & Richstone, D. 1992, *ApJ*, 393, 559
- Kormendy, J., & Richstone, D. 1995, *ARA&A*, 33, 581 (KR95)
- Kormendy, J., & Westpfahl, D. J. 1989, *ApJ*, 338, 752
- Lauer, T. R. 1985, *ApJS*, 57, 473
- Lauer, T. R., *et al.* 1995, *AJ*, 110, 2622
- Lauer, T. R., *et al.* 1997, in preparation
- Leach, R. 1981, *ApJ*, 248, 485
- Michard, R., & Simien, F. 1988, *A&AS*, 74, 25
- Miyoshi, M., *et al.* 1995, *Nature*, 373, 127
- Moffat, A. F. J. 1969, *A&A*, 3, 455
- Morgan, W. W., & Keenan, P. C. 1973, *ARA&A*, 11, 29
- Nieto, J.-L., & Bender, R. 1989, *A&A*, 215, 266
- Nieto, J.-L., Capaccioli, M., & Held, E. V. 1988, *A&A*, 195, L1
- Nieto, J.-L., Poulain, P., Davoust, E., & Rosenblatt, P. 1991, *A&AS*, 88, 559
- Peletier, R. F., Davies, R. L., Illingworth, G. D., Davis, L. E., & Cawson, M. 1990, *AJ*, 100, 1091
- Persson, S. E., Frogel, J. A., & Aaronson, M. 1979, *ApJS*, 39, 61
- Pierce, M. 1991, private communication
- Poulain, P. 1988, *A&AS*, 72, 215
- Qian, E. E., de Zeeuw, P. T., van der Marel, R. P., & Hunter, C. 1995, *MNRAS*, 274, 602
- Richstone, D., *et al.* 1998a, in preparation
- Richstone, D., *et al.* 1998b, in preparation
- Salmon, D. 1985, *CFHT Info. Bull.*, No. 13, 9
- Sandage, A. 1961, *The Hubble Atlas of Galaxies* (Washington, Carnegie Institution of Washington)
- Sandage, A., Freeman, K. C., & Stokes, N. R. 1970, *ApJ*, 160, 831
- Sandage, A., & Visvanathan, N. 1978, *ApJ*, 223, 707
- Sargent, W. L. W., Schechter, P. L., Boksenberg, A., & Shortridge, K. 1977, *ApJ*, 212, 326
- Schechter, P. L., & Gunn, J. E. 1979, *ApJ*, 229, 472

- Scorza, C., & Bender, R. 1995, *A&A*, 293, 20
- Stover, R. J. 1988, in *Instrumentation for Ground-Based Optical Astronomy: Present and Future*, ed. L. B. Robinson (New York: Springer-Verlag), 443
- Strom, S. E., Strom, K. M., Goad, J. W., Vrba, F. J., & Rice, W. 1976, *ApJ*, 204, 684
- Tody, D., *et al.* 1986, *IRAF User Handbook*, Tucson, National Optical Astronomy Observatories
- Tonry, J. L. 1984, *ApJ*, 283, L27
- Tonry, J. L. 1987, *ApJ*, 322, 632
- Tremblay, B., & Merritt, D. 1995, *AJ*, 110, 1039
- Tully, R. B. 1988, *Nearby Galaxies Catalog* (Cambridge: Cambridge University Press)
- van den Bosch, F. C., & Jaffe, W. 1997, in *The Nature of Elliptical Galaxies*, ed. M. Arnaboldi, G. S. Da Costa, & P. Saha (San Francisco: ASP), 142
- van der Marel, R. P., Cretton, N., de Zeeuw, P. T., & Rix, H.-W. 1997b, *ApJ*, submitted
- van der Marel, R. P., de Zeeuw, P. T., Rix, H.-W. 1997, *ApJ*, in press
- van der Marel, R. P., de Zeeuw, P. T., Rix, H.-W., & Quinlan, G. D. 1997a, *Nature*, 385, 610
- van der Marel, R. P., Evans, N. W., Rix, H.-W., White, S. D. M., de Zeeuw, T. 1994b, *MNRAS*, 271, 99
- van der Marel, R. P., & Franx, M. 1993, *ApJ*, 407, 525
- van der Marel, R. P., Rix, H.-W., Carter, D., Franx, M., White, S. D. M., de Zeeuw, T. 1994a, *MNRAS*, 268, 521
- Walker, G. A. H., *et al.* 1984, in *State-of-the-Art Imaging Arrays and Their Applications*, ed. K. N. Prettyjohns, *Proc. SPIE*, 501, 353
- Webb, C. J. 1964, *AJ*, 69, 442
- Whitmore, B. C., McElroy, D. B., & Tonry, J. L. 1985, *ApJS*, 59, 1